

Supporting Information

Tunable DNA Origami Motors Translocate Ballistically Over μm Distances at nm/s Speeds

Alisina Bazrafshan, Travis A. Meyer, Hanquan Su, Joshua M. Brockman, Aaron T. Blanchard, Selma Piranej, Yuxin Duan, Yonggang Ke, and Khalid Salaita**

anie_201916281_sm_miscellaneous_information.pdf

anie_201916281_sm_file_1.pptx

anie_201916281_sm_Movie_S1.mov

anie_201916281_sm_Movie_S2.mov

anie_201916281_sm_Movie_S3.mov

Author Contributions

A.B. Conceptualization: Lead; Data curation: Lead; Formal analysis: Lead; Funding acquisition: Supporting; Investigation: Lead; Methodology: Lead; Software: Lead; Supervision: Lead; Validation: Lead; Visualization: Lead; Writing - Original Draft: Lead; Writing - Review & Editing: Lead

T.M. Investigation: Supporting; Methodology: Supporting; Validation: Equal; Writing - Original Draft: Equal

H.S. Methodology: Supporting; Validation: Supporting; Visualization: Supporting

J.B. Formal analysis: Supporting; Software: Supporting; Visualization: Supporting; Writing - Review & Editing: Supporting

A.B. Software: Supporting; Validation: Supporting

S.P. Data curation: Supporting; Methodology: Supporting; Validation: Supporting

Y.D. Investigation: Supporting; Validation: Supporting

Y.K. Conceptualization: Lead; Funding acquisition: Supporting; Investigation: Supporting; Project administration: Supporting; Resources: Supporting; Supervision: Lead; Validation: Supporting; Visualization: Supporting; Writing - Original Draft: Supporting; Writing - Review & Editing: Supporting

K.S. Conceptualization: Lead; Funding acquisition: Lead; Investigation: Supporting; Methodology: Supporting; Project administration: Lead; Resources: Lead; Supervision: Lead; Validation: Supporting; Visualization: Supporting; Writing - Original Draft: Lead; Writing - Review & Editing: Lead.

Table of Contents

1. <i>Materials and Methods</i>	3
2. <i>Design of 16 helix bundle DNA origami motor</i>	8
4. <i>DNA origami motor fluorescence characterization</i>	12
5. <i>Quantification of fraction of RNA lost in depleted tracks</i>	13
6. <i>Fluorescence tracking of 16HB motors</i>	14
7. <i>Effect of enzyme concentration on 16HB motor</i>	19
8. <i>Kinetic measurements of RNase H activity</i>	20
9. <i>Synthesis of spherical motors</i>	22
10. <i>Analyses of width and length of depleted tracks</i>	23
11. <i>Generation of geometric mutants</i>	25
12. <i>Modelling of 16HB motors</i>	26
13. <i>Tuning the flexibility of 16HB motors</i>	35
14. <i>Generation and analyses of polyvalency/density mutants</i>	38
15. <i>Comparison of 16HB with other nanoscale motors</i>	43
16. <i>Oligonucleotides used in this study</i>	44
17. <i>Captions for supplementary movies</i>	51
18. <i>References</i>	52

1. Materials and Methods

All chemicals were purchased from Sigma-Aldrich unless otherwise noted. Stock solutions were made using Nanopure water (Barnstead™ Nanopure™ system, resistivity = 18.2 MΩ, Thermofisher, Waltham, MA), herein referred to as DI water. All oligonucleotides were custom synthesized by Integrated DNA Technologies (Coralville, IA) and are summarized in Tables S2-S5. RNase H was obtained from Takara Clontech (Product No. 2150A). All motor translocation measurements were performed in IBIDI sticky-Slide VI^{0.4} 17 × 3.8 × 0.4 mm channels. Teraspek™ Microspheres, 0.1 μm Catalog number T7279 were purchased from Thermofisher. Azido-PEG4-NHS ester was purchased from Click Chemistry Tools (Scottsdale, AZ, product# AZ103-1000). Purelink™ RNase A was purchased from Thermofisher (Waltham, MA, product# 12091021).

Optical microscopy

A Nikon *Ti Eclipse* microscope was used for all TIRF experiment and kinetic assays for surface optimization. The microscope was equipped with an Intensilight epifluorescence source (Nikon), a CFI Apo 100 × NA 1.49 objective (Nikon), and a TIRF launcher with three laser lines: 488 nm (10 mW), 561 nm (50 mW), and 638 nm (20 mW). The microscope also included a Nikon Perfect Focus System, which allows the capture of multipoint and time-lapse images without loss of focus. Motion experiments of 16HB motors were performed in two channels and were obtained using the Quad Cube (product# 97327), TRITC (product #96321) filter cube set supplied by Chroma. Using the ND acquisition toolbox in the Elements software package, one fluorescence image with each cube was captured every 30 seconds for a total duration of 75 minutes. The images were collected at 16-bit depth using an Andor EMCCD iXON DU897 512x512 camera. All imaging was conducted at room temperature.

A Nikon Ti2 microscope was used to capture wide field fluorescence images of depletion tracks after the time lapse to quantify percent fluorescence loss during motor motion and Kuhn segment analyses. This microscope was equipped with SOLA SE Light Engine® and Nikon Perfect Focus System. The images were collected at 16-bit depth using Prime 95B 25mm™ Scientific CMOS 1608x1608 Camera (Photometrix, AZ).

Super-resolution imaging (SIM) of the fluorescence-depletion tracks

SIM images were acquired on a Nikon N-SIM system equipped with a CFI Apo ×100 1.49 NA objective and an Andor iXon EMCCD (60 nm per pixel). For each N-SIM image, nine images of a 3'-Cy3-RNA sample were acquired in different phases using a 561 nm laser as an excitation source and were reconstructed using the Nikon Elements software package.

Transmission Electron Microscopy

TEM images were collected using a Hitachi HT-770 microscope operating at 80kV with magnification between 15000x and 70000x. Negative-stain TEM images were collected by staining prepared grids with 1% uranyl formate for 30 seconds.

Fabrication of RNA monolayers

A #1.5 glass slide (25 × 75 mm) was cleaned by sonication in DI (18.2 MΩ cm⁻¹) water for 15 minutes. The sample was then subjected to a second sonication in 200 proof ethanol for 15 minutes and was subsequently dried under a stream of N₂. The glass slide was etched by

piranha solution (v/v = 3:7 hydrogen peroxide/sulfuric acid, please take caution as piranha is extremely corrosive and may explode if exposed to organics) for 30 min to remove residual organic materials and activate hydroxyl groups on the glass. The cleaned substrates were rinsed with DI water in a 200 mL beaker for 6 times and further washed with ethanol thrice. Slides were then transferred to a 200 mL beaker containing 2% (v/v) APTES in ethanol for 1 h, washed with ethanol thrice and thermally cured in an oven (~110°C) for 10 min. The slides were then mounted to 6-channel microfluidic cells (Sticky-Slide VI 0.4, Ibidi). To each channel, ~50 μ L of 10 mg/mL of NHS-PEG₄-azide (Click Chemistry Tools) in 0.1 M NaHCO₃ (pH = 9) was added and incubated for 2h. The channels were washed with 1 mL DI water thrice and the remaining water in the channels was removed by pipetting. After thoroughly rinsing the surface with DI water, a solution of 10 μ M alkyne modified DNA (anchor strand), 50 μ M THTPA, 10 μ M CuSO₄ and 1 mM sodium ascorbate in 1 M potassium phosphate buffer was added to the surface and incubated for 1 hour. After incubation, excess DNA was removed from the channel using a ~5 ml DI water rinse. Lastly, the RNA substrate was immobilized to the surface through hybridization by adding a 100 μ l of a complementary RNA/DNA chimera (100 nM) in 1 \times PBS for 12 hours at room temperature. The wells were sealed with Parafilm for each step to prevent evaporation and the resulting RNA monolayer remained stable for weeks, as determined by fluorescence imaging.

Determining RNA surface density

RNA surface density was measured by releasing the Cy3-tagged RNA from the surface by adding 100 μ l of RNase A (10 μ g ml⁻¹ in 1 \times PBS) and then quantifying the Cy3 fluorescence intensity in solution using a calibration curve obtained with the fluorescence microscope.

Synthesis, purification, and characterization of 16HB origami structures

Single-stranded scaffold p7560 was prepared from M13 phage using a previously reported method [1]. A 16HB rod was designed in caDNAo [2], based on a 4x4 square lattice cross-section. To synthesize 16HB, a 10-fold excess of staple strands were mixed with p7560 scaffold strand (10 nM) in folding buffer (5 mM Tris, 1 mM EDTA, 10 mM MgCl₂ with a total volume of 50 μ L. The mixture was denatured at 85°C for 10 minutes, followed by a slow anneal from 60°C to 25°C over 18 hours (-1°C/30 minutes). 16HB were purified from excess staples using agarose gel electrophoresis (0.67%) in 0.5 \times TBE+Mg buffer (45 mM Tris, 45 mM boric acid, 1 mM EDTA, 10 mM MgCl₂). AlexaFluor647 tagged cargo strands were subsequently added at 32x excess and the mixture was incubated at room temperature for at least 3 hours before experiments. 16HB structures were characterized by agarose gel electrophoresis (1.5%) and negative stain TEM imaging (1% uranyl formate).

Determination of RNase H surface kinetics

The RNA monolayer was incubated with 100 μ L of solution containing 100 nM complementary DNA in 1X PBS overnight. The following morning, different solutions containing different buffers and concentrations of RNase H were added to the surface. An automated time lapse was programmed to collect one fluorescent image every minute using the 100x oil objective (1.49 NA). Using the fluorescence calibration curve, we determined the absolute molecular density of the RNA monolayer during the kinetic run. After correcting for photobleaching using data from a time lapse without addition of RNase H, the data was fitted to an exponential decay function to report the half-life.

16HB motor translocation powered by RNase H

Initially, RNA surfaces were washed with 3 mL of PBS to remove excess unbound RNA. Next, DNA origami motors were hybridized to the RNA substrate. Briefly, 1 μL of purified DNA origami particles were diluted with 1X RNase H buffer (3 mM MgCl_2 , 50 mM Tris-HCl, pH = 8.3) buffer to generate a 10 pM concentration. 50 μL of that solution was then added to the RNA substrate (in an ibidi microchannel). Hybridization between the particles and the complementary RNA monolayer occurred over an incubation period of 2-5 minutes (Movie S1). After hybridization, excess particles and excess AF647 tagged cargo strands were washed using 1 mL of RNase H buffer. Next, a solution of tetraspek beads was added for 3-5 min, and the unbound beads were washed with 1 mL of RNase H buffer. These beads were important for drift correction. Afterwards, motor translocation was initiated by buffer exchange with 100 μL of RNase H reaction buffer (0.9X RNase H buffer, 1 mM DTT, 5% v/v formamide) that included different concentrations of RNase H from an enzyme stock of 1.4 μM enzyme.

Synthesis of spherical motors

Modification of 50 nm gold nanoparticles with thiolated DNA was achieved using a recently published method^[3]. Briefly, 20 μL of 100 μM thiolated DNA was added to 180 μL of a solution of commercially purchased 50 nm diameter gold nanoparticles from Sigma-Aldrich (Cat # 753645) in DI water in a glass vial. The mixture was cooled (in a -30 freezer) for 15 min to freeze the solution. Subsequently, the 200 μL solution was allowed to thaw at room temperature for 30 min. Freeze-thaw cycles were repeated three times. Then, via centrifugation at 5000 rpm for 8 minutes, the mixture was washed with 1 mL of 1X PBS three times. The resulting modified DNA-AuNPs were stable for use for at least one week.

Quantification of DNA density in 50 nm spherical motors

We quantified the number of DNA strands per gold nanoparticle by releasing the DNA from the gold nanoparticles and measuring the released fluorescence. DNA particle solutions were prepared by diluting a 4 nM stock solution to 0.04 nM with TE buffer. The DNA on the particle was released by dissolving the gold with potassium cyanide (KCN, please take caution: tune the pH of the buffer to basic as KCN solutions in acidic buffers can generate lethal HCN fumes!!!). This was performed by adding 1 μL of a 5 M stock solution of KCN to the mixture. The samples were incubated with KCN for 30 min to ensure complete dissolution. The loss of red color was complete within 10 minutes and confirmed by gold dissolution. We then prepared a calibration curve containing 0, 0.1, 1, 10, 50 and 250 nM of thiolated DNA-FAM in 1x TE buffer and 50 mM KCN. KCN was included in the calibration wells to ensure an accurate calibration curve and blank subtraction. After complete dissolution of the gold nanoparticles, fluorescence intensities (485/528 nm excitation/emission) of each well were then measured using a Bio-Tek Synergy HT plate reader to determine the concentration of DNA released from the particles. This amount was divided by the concentration of the 50 nm gold nanoparticles (measured by UV-VIS Max abs = 535 nm, Extinction coefficient = $1.72 * 10^{10} \text{ M}^{-1} \text{ cm}^{-1}$) to yield the number of oligonucleotides per gold nanoparticle.

Gold nanoparticle translocation by RNase H

Initially, RNA surfaces were washed with 3 ml of PBS to remove excess unbound RNA. Next, a solution containing 10 pM of DNA-gold nanoparticles in 1X RNase H buffer were hybridized to the RNA substrate. Hybridization between the particles and the complementary RNA monolayer

occurred over an incubation period of 2 minutes. After hybridization, excess particles were washed using 1 mL of RNase H buffer. Motor translocation was then initiated by buffer exchange with 100 μ l of RNase H reaction buffer (0.5X RNase H buffer, 10 μ M DTT, 10 % v/v formamide and 0.75% v/v triton X) which included different concentrations of RNase H from an enzyme stock of 1.4 μ M enzyme. The example brought in Figure S13 was obtained with 2.5 units of enzyme (72 nM). Gold nanoparticle motion was measured using timelapse imaging of the reflection interference contrast microscopy (RICM) channel at a frequency of 1 image per 5 seconds. using the Nikon software package to acquire an RICM image every 5 seconds. Particle tracking was achieved using MOSAIC ImageJ plugin^[4]. The MOSAIC plugin outputs a table which is transferred to MATLAB using a custom script for motion analysis.

Image processing

Image processing was performed in Fiji (ImageJ), MATLAB 2018b (MathWorks) and in Picasso, a software package that is freely available via the Jungmann lab website^[5]. The bioformats toolbox enabled direct transfer of Nikon Elements image files (.nd2) into the MATLAB environment. A custom MATLAB code enabled transfer of hdf5 data files from Picasso.

The search area used in Picasso localization was set to 7 pixels. The x and y trajectories of at least 3 fiducial markers in the field of view was subtracted from all motor trajectories in Picasso to account for x - y stage drift (Figure S7). Next, using the Picasso filter, the localizations of fiducial markers were deleted based on an intensity cut off filter. All drift corrected 647 localizations were clustered into individual trajectories based on their x and y position. A given trajectory was used in subsequent analysis only if the following three conditions were met: 1) the motor brightness intensity was within a specific range of values that were obtained from control experiments (Figure S7). This intensity cutoff helped distinguish completely formed 16HB from fiducial markers, incomplete 16HBs and background noise. 2) The trajectory was detectable for at least 60 mins (120 frames). 3) The trajectory only included a single 16HB motor.

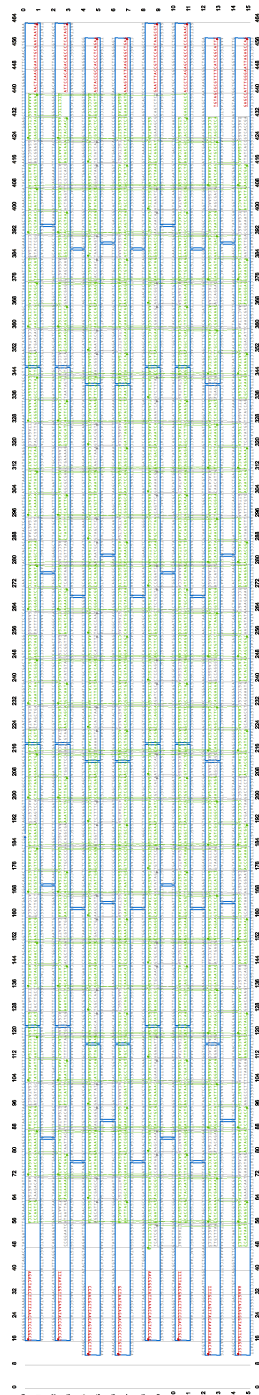
Fluorescence images of depletion tracks were analyzed by MATLAB or ImageJ. All images for quantitative processes were background subtracted. Each line scan was averaged across at least three pixels (unless otherwise noted) adjacent to the line to reduce the influence of noise peaks.

Trajectory analysis

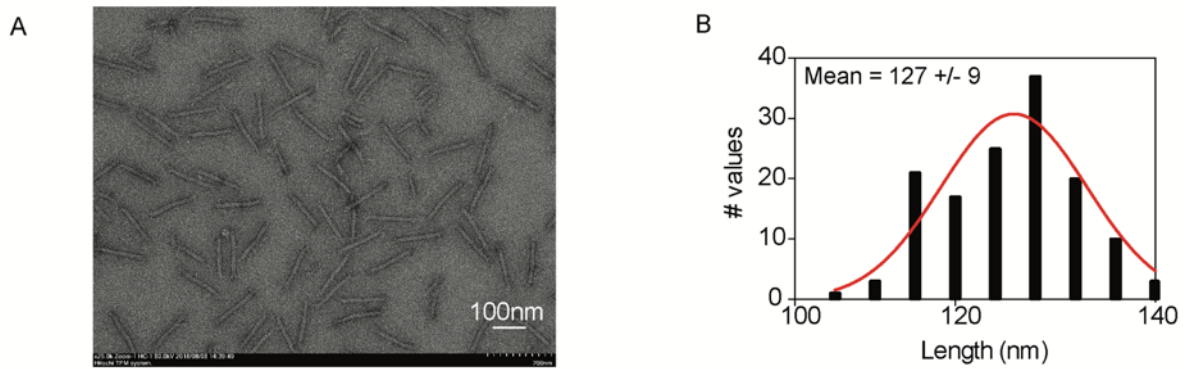
All individual drift corrected 16HB trajectories were subjected to a smoothing function that averaged 5 consecutive localizations to reduce lateral noise (Figure S8). The first 120 x and y positions of each trajectory were selected as a one-hour acquisition. The Euclidean distance between the first and last position was reported as the net displacement of each 16 HB. The summation of the Euclidean distances between every two consecutive locations was reported as the distance travelled. The division of each Euclidean distance by 0.5 mins (time between two consecutive frames) was reported as instantaneous velocity. A linear fit to the distance travelled vs time plots was reported as average velocity. The alpha values were calculated by plotting the mean square displacement vs lag times. Lag time is the time difference between each two location coordinates for a single trajectory. Hence, there will be 120 mean square displacements

for lag time 0.5 min, 119 for lag time 1 and 1 for lag time = 60 min. The slope of a log-log fit to the MSD vs lag time plot for each trajectory was reported as the alpha value. To enhance the robustness of the fit, the fit was programmed to take into account lag times 0.5 to 30 min. The alpha value was reported only if the R^2 of the fit was greater than 0.9.

2. Design of 16 helix bundle DNA origami motor

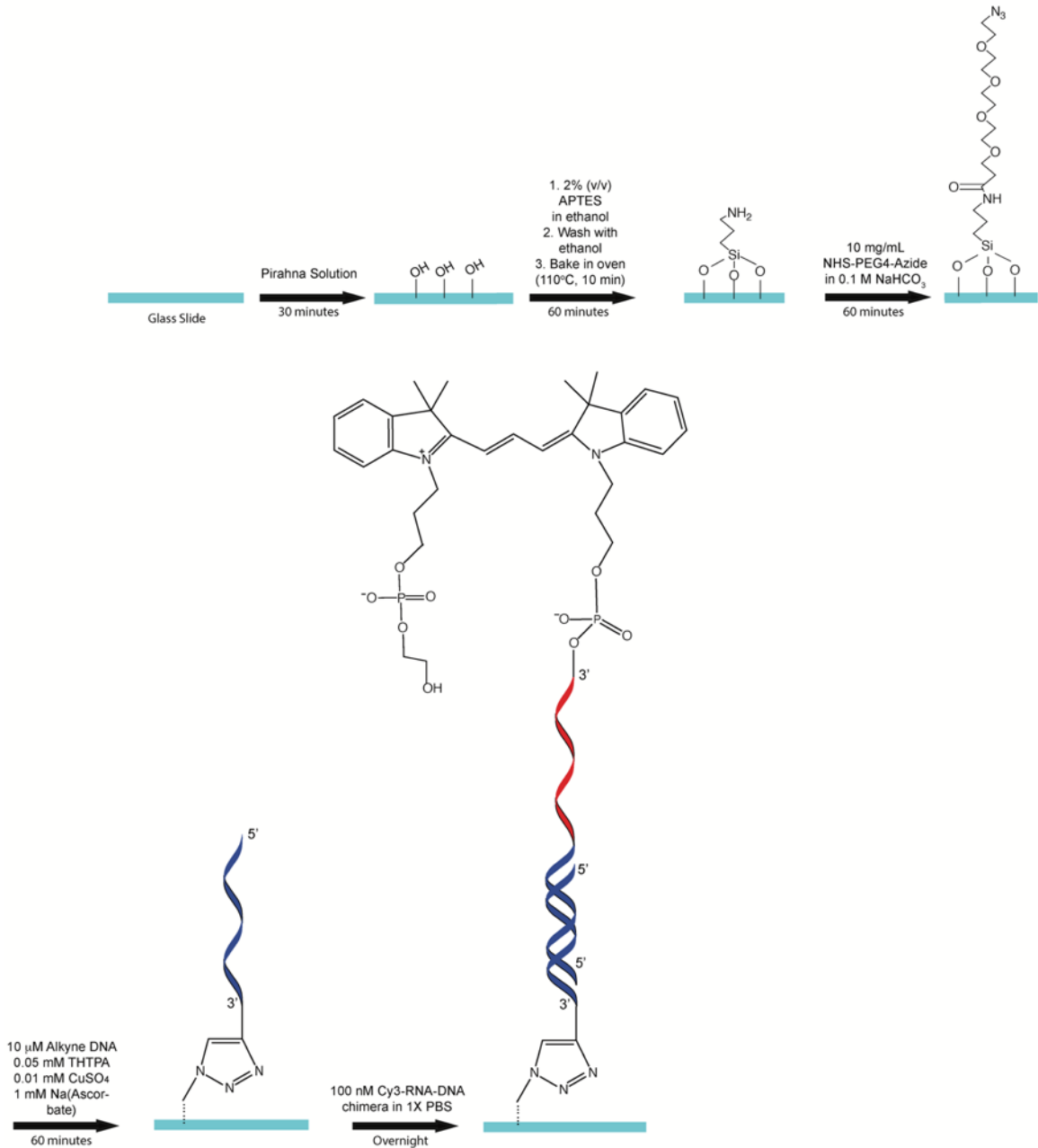


Supplementary Figure 1. Schematic of the 16HB design as generated by caDNAno. Blue: p7560 scaffold strand, Grey: Blank staple strands, Green: Staples with RNA-binding extensions Red: Cargo-carrying strands. Additional design information showing full staple sequences can be found in Table S4.

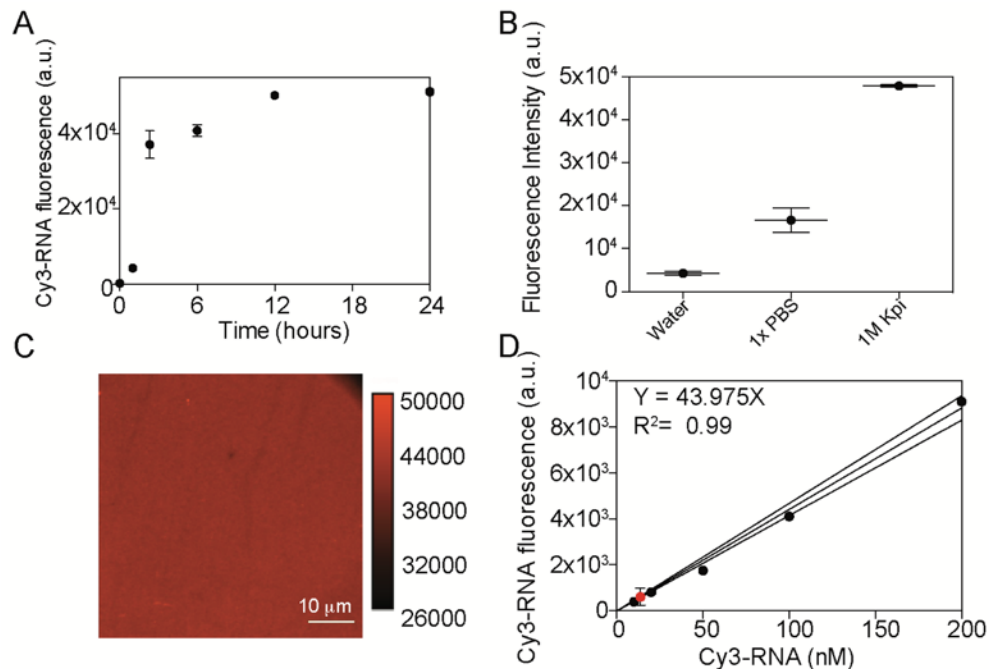


Supplementary Figure 2. (A) TEM image of 16HB DNA origami structures. (B) Histogram of 16HB lengths measured from TEM. $n = 137$ origami structures that were synthesized from two different synthesis batches.

3. Cy3-RNA monolayer synthesis and characterization

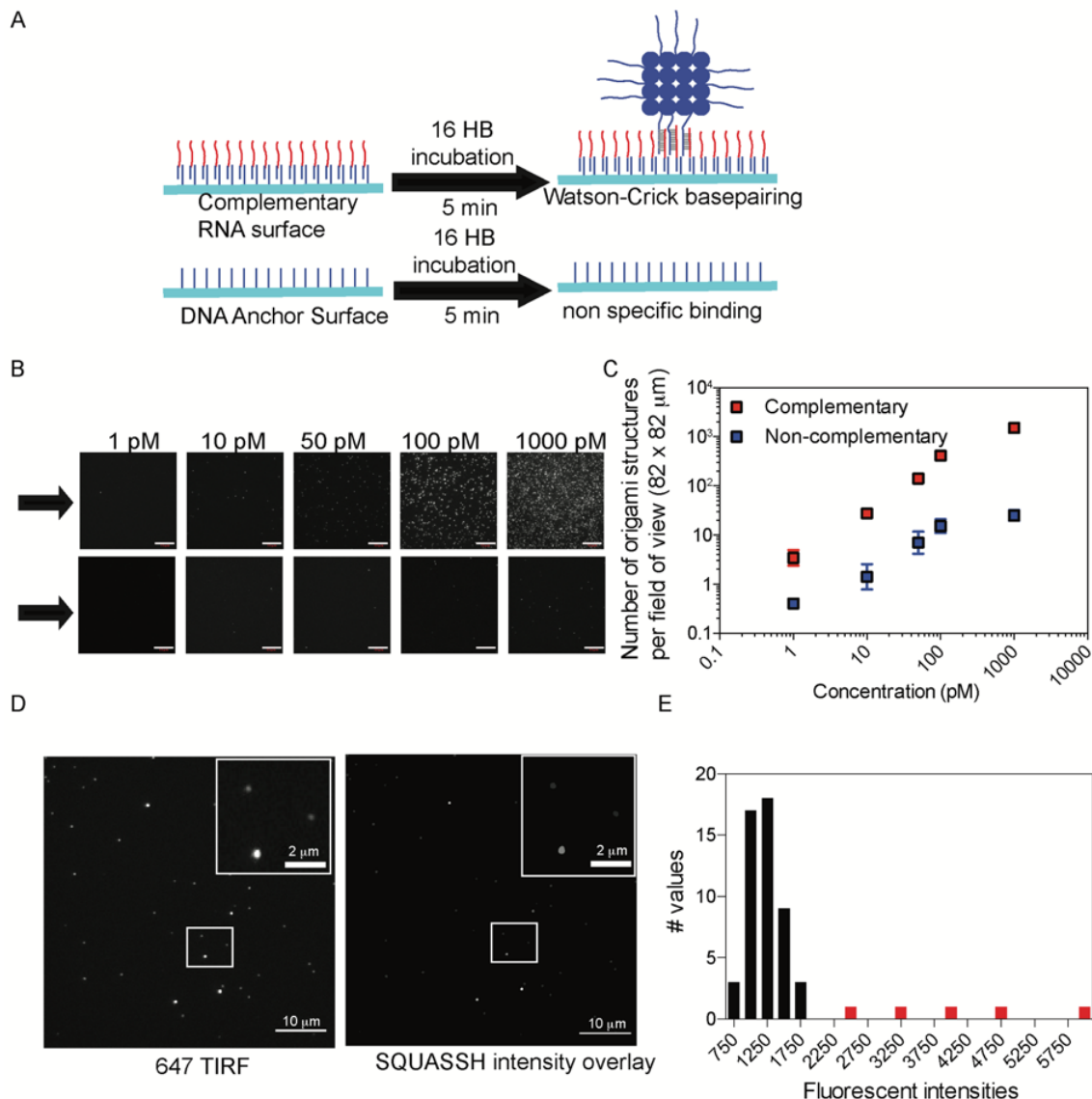


Supplementary Figure 3. Schematic of the surface preparation steps used for preparing RNA monolayer surfaces. The red color indicates RNA sequence, while blue indicates DNA.



Supplementary Figure 4. Characterization of RNA surface. (A) Time dependent quantification of hybridization between 3'Cy3-RNA (100 nM) and surface immobilized DNA anchor strand in 1x PBS. Error bars represent the standard deviation in the average fluorescence intensity from at least 5 regions across each channel. An increase in fluorescence intensity is indicative of an increase in the surface density of RNA that is due to greater hybridization. Near saturation is typically observed after ~6 hrs of hybridization. The fluorescence intensity was used as a quality control to ensure that the surfaces were properly prepared, and the RNA density was sufficiently high. (B) Optimization of conditions to maximize yield of click reaction between alkyne modified anchor DNA and the azide-modified surface. Three buffer conditions were scanned for optimization of click chemistry: water, 1x PBS buffer and 1M phosphate buffer. Increasing salt concentration of the buffer led to a denser DNA monolayer which then translates to an increase in fluorescence intensity as a result of hybridization to the RNA/DNA chimera. (C) Representative Cy3 image after 12 hours of hybridization and washing excess RNA. (D) RNA density was then quantified by releasing the immobilized 3'Cy3-RNA from the surface by addition of 1 μg RNase A and measuring the resulting fluorescence with the optical microscope. The amount of RNA released was quantified using a fluorescence calibration curve by measuring the fluorescence intensity of known concentrations of Cy3-RNA under identical conditions. The amount of released immobilized RNA (red) is divided by the surface area of the IBIDI channel (79.7 mm²) to determine the average RNA surface density in units of molecules/μm² which equaled 22000/μm² ± 4000. Error bars show the SEM of 3 independent experiments.

4. Characterization of 16HB surface binding

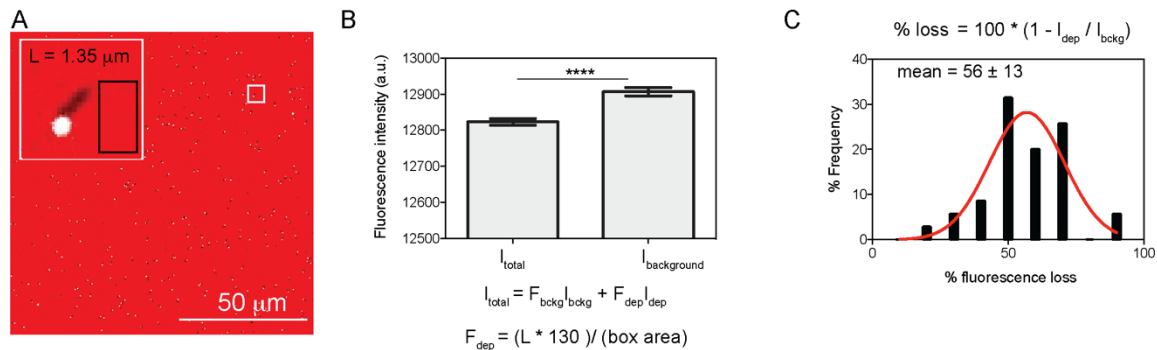


Supplementary Figure 5. Origami binding is driven by specific Watson-Crick base pairing.

(A) Schematic showing experimental design. The surface was washed with PBS after each incubation to remove excess unbound structures. (B) Representative Alexa 647 TIRF images of surfaces prepared according to the schematic shown in (A). (C) A plot of particle count vs concentration of 16HB origami incubated on the RNA monolayer. Particle count was obtained using the SQUASSH toolbox^[6]. Error bars represent the standard deviation of particle counts in 5 different regions of interest along the microchannel (many of the data points have error bars that are smaller than the symbol). Red indicates particle incubation on an RNA monolayer and blue represents incubation on a non-complementary DNA monolayer. Note that the non-complementary DNA strand is the aminated DNA anchor. (D) TIRF 647 image and SQUASSH analysis of 16 HB tagged with 16 AF647 cargo strands and tetraspek beads. (E) Histogram of 16HB intensities (black) along with tetraspek beads (red). Tetraspek beads (red) have a much higher intensity compared to the 16HB origami structures.

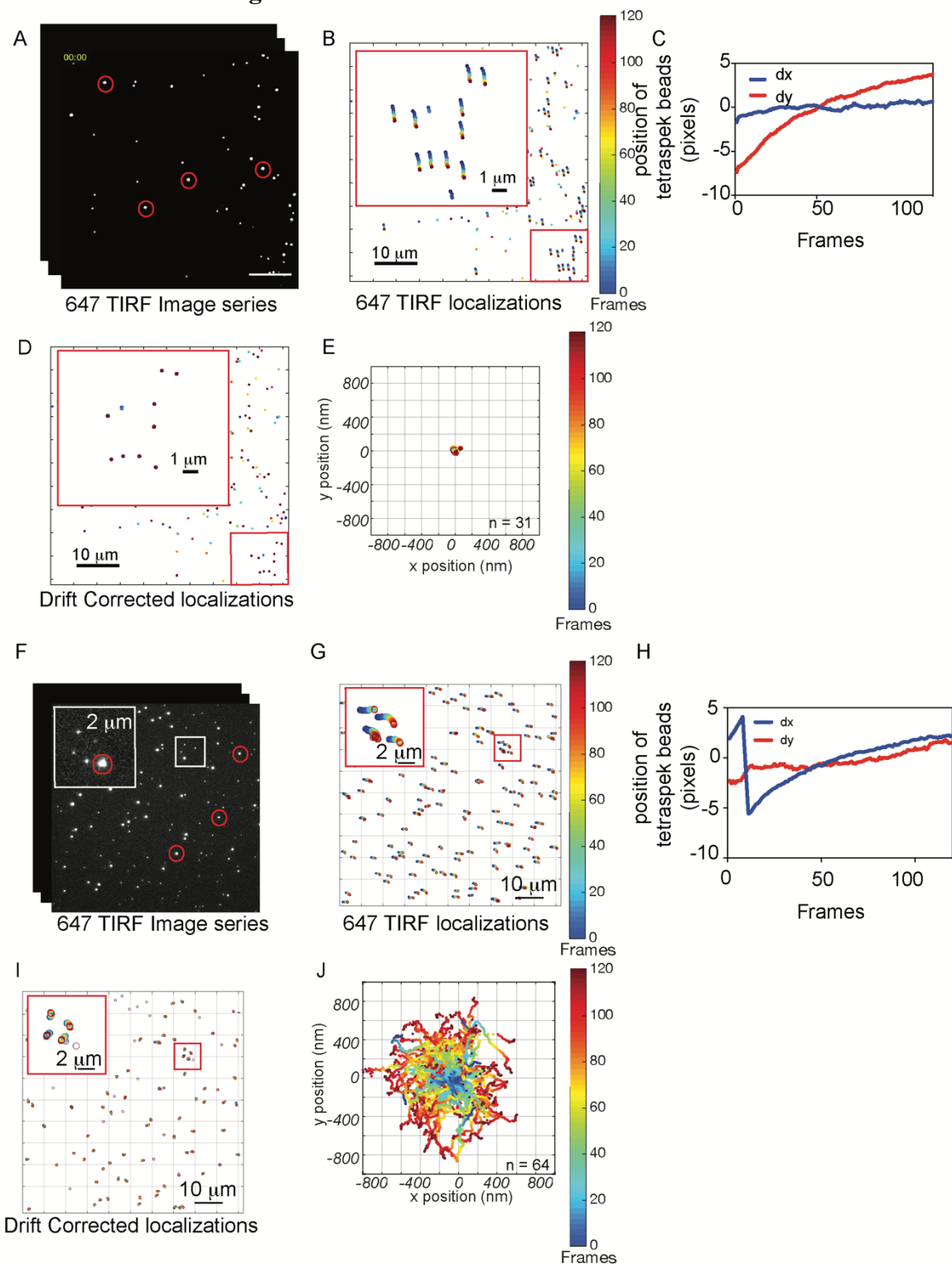
5. Quantification of RNA hydrolysis in depleted tracks

We calculated the fraction of RNA lost in depletion tracks by first drawing a box such as the one shown in white in Figure S6A around a given depletion track. We measured the average intensity of the whole box (I_{total}) and the average intensity of the background from the same box (I_{bckg})-intensity of a box such as the one shown in black in Figure S6A. Given that $I_{total} = F_{dep}I_{dep} + F_{bckg}I_{bckg}$ where F_{dep} and F_{bckg} are fraction of the area of box corresponding to the depletion track and background respectively, we can calculate the average intensity of depletion tracks by assuming $F_{dep} = (130 * \text{length}_{depletion}) / (\text{box area})$ and $F_{bckg} = 1 - F_{dep}$. Percentage of RNA lost in each depletion track was calculated by $(1 - (I_{dep}/I_{bckg})) * 100$. This analysis was done on linear tracks only because we assume the area of depletion is a rectangle with width 130 nm (from SIM).



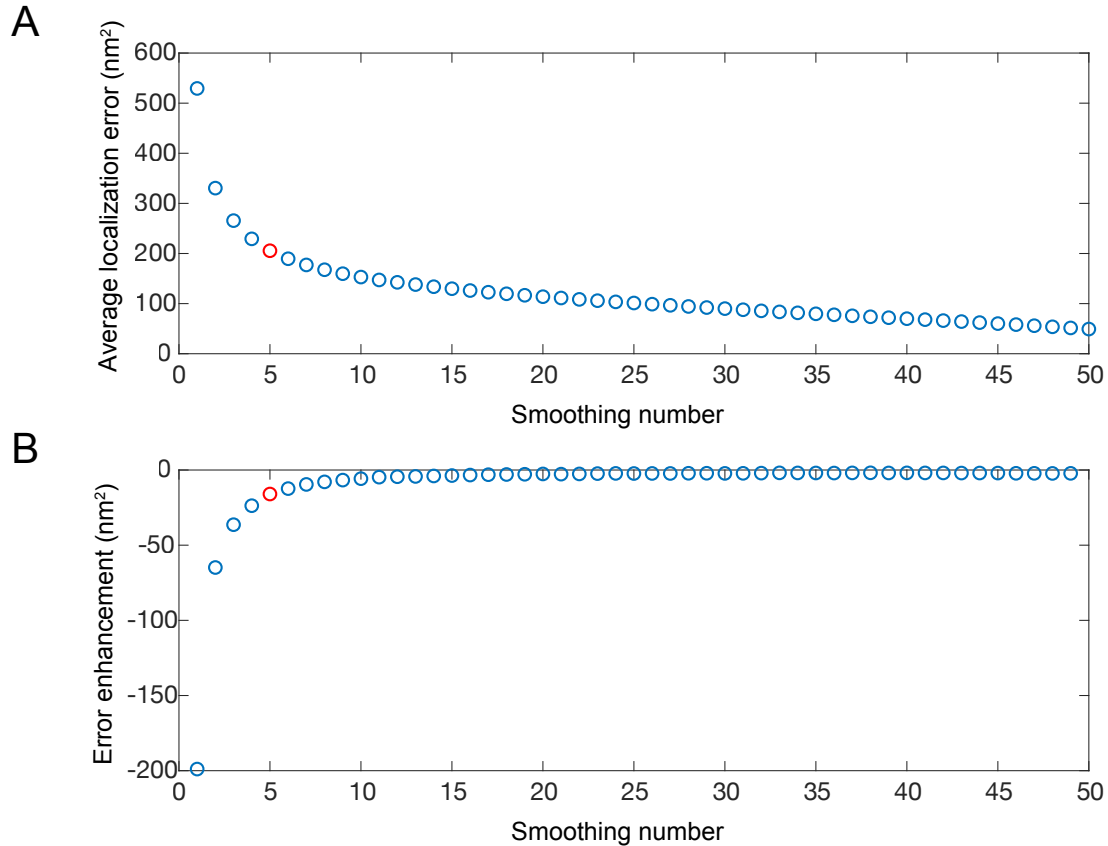
Supplementary Figure 6. Quantification of fraction of RNA lost in depletion tracks. (A) Representative overlay image of Cy3 fuel and AF647 16HB. Red indicates the intensity of Cy3 and white is the AF647 signal intensity. The lengths of the depletion tracks were measured manually in imageJ. (B) A bar plot comparing the average fluorescence of the box (I_{total}) and the average fluorescence of background (I_{bckg}). I_{bckg} was measured by averaging the intensity of the pixels within the black box shown in (A). The error bars represent 95% confidence intervals based on the variations of intensities of pixels used to report each average. **** means $p < 0.0001$ (C). A histogram plot of % fluorescence loss in each track for $n = 35$ from two independent surfaces.

6. Fluorescence tracking of 16HB motors

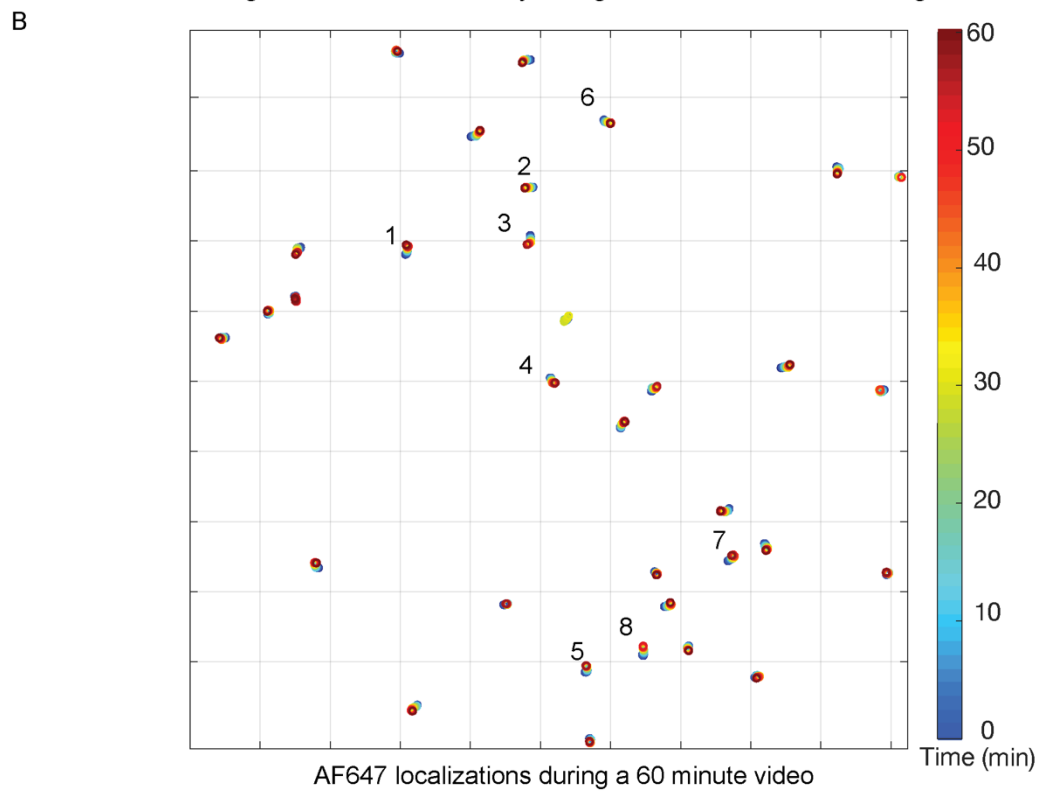
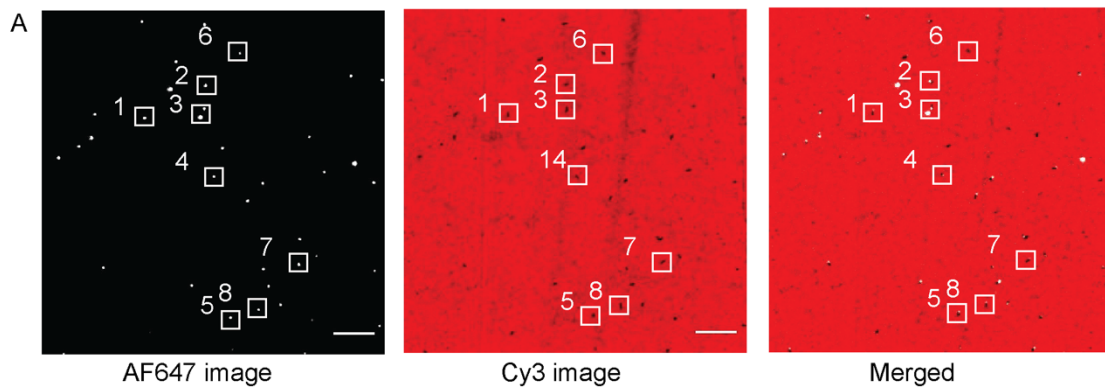


Supplementary Figure 7. Extracting super-resolution position information. (A) TIRF647 image series were collected at regions of interest containing tetraspek beads and 16HB origami structures. Four of the tetraspek beads used for drift-correction are marked with a red circle. (B) Picasso software localizations of the origami structures and the tetraspek beads were obtained for

every frame and were plotted on a xy coordinate. (C) The average drift of the microscope stage was obtained by averaging the trajectories of the tetraspek beads (D) The drift corrected trajectories of the negative control sample showed that the 16HB structures remain immobile. (E) All trajectories of 16HB structures were plotted from the center of the coordinate system ($n = 31$). (F-J) are identical to (A-E) but with the addition of RNase H. Note that J shows the trajectory of $n = 64$ motors.

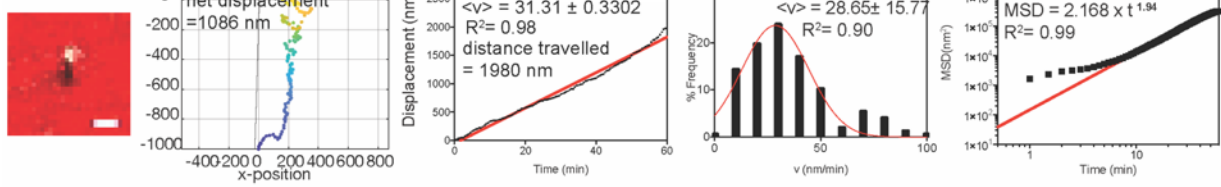


Supplementary Figure 8. Optimization of smoothing number. (A) Average localization error for 50+ origami structures without RNase H plotted as a function of smoothing number. Larger smoothing numbers improve the precision in localization but reduce time resolution. (B) A plot of the first derivative of localization error as a function of smoothing number. It shows that a minimal enhancement is gained in precision when the smoothing number is greater than 5.

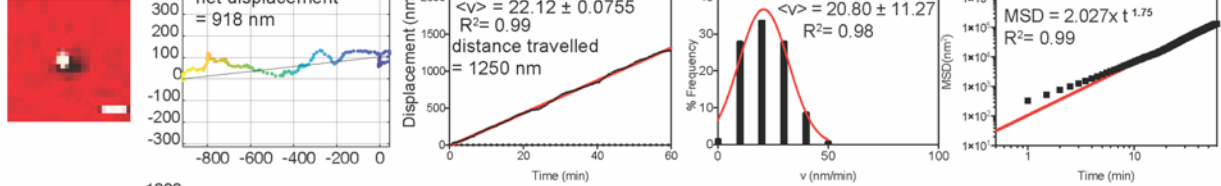


C

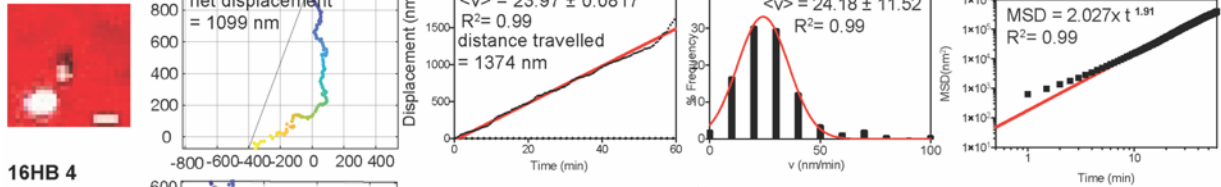
16HB 1



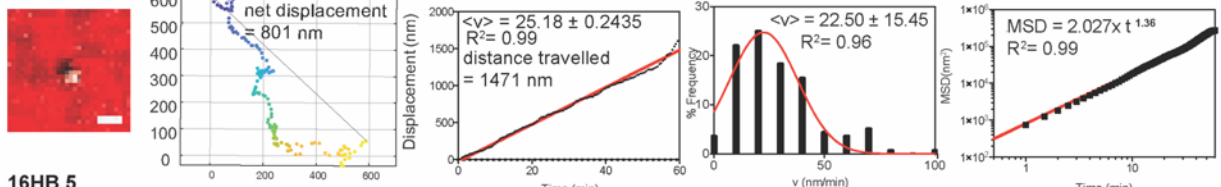
16HB 2



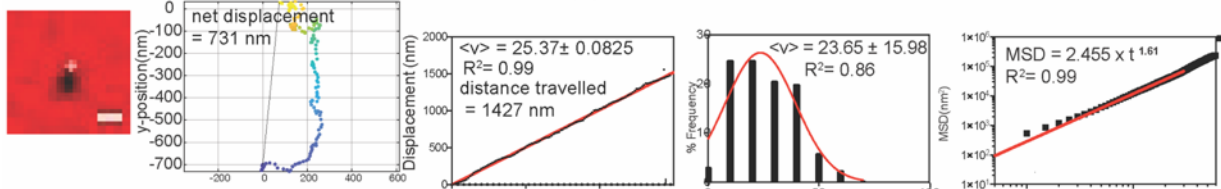
16HB 3



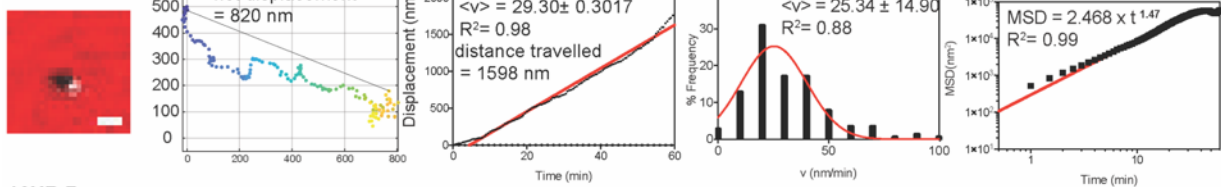
16HB 4



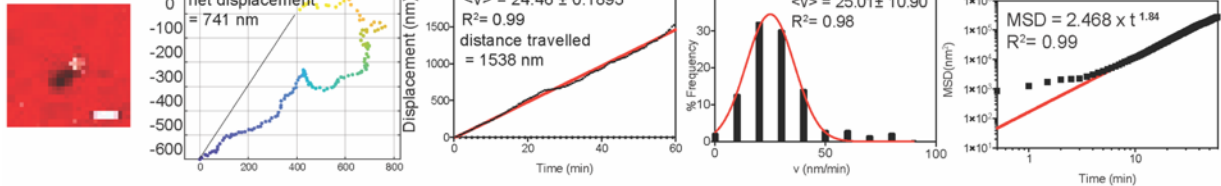
16HB 5



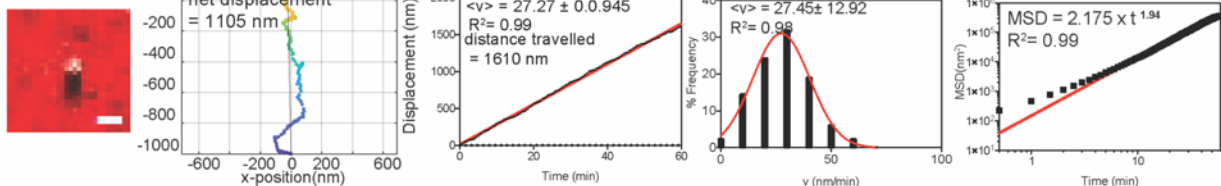
16HB 6



16HB 7

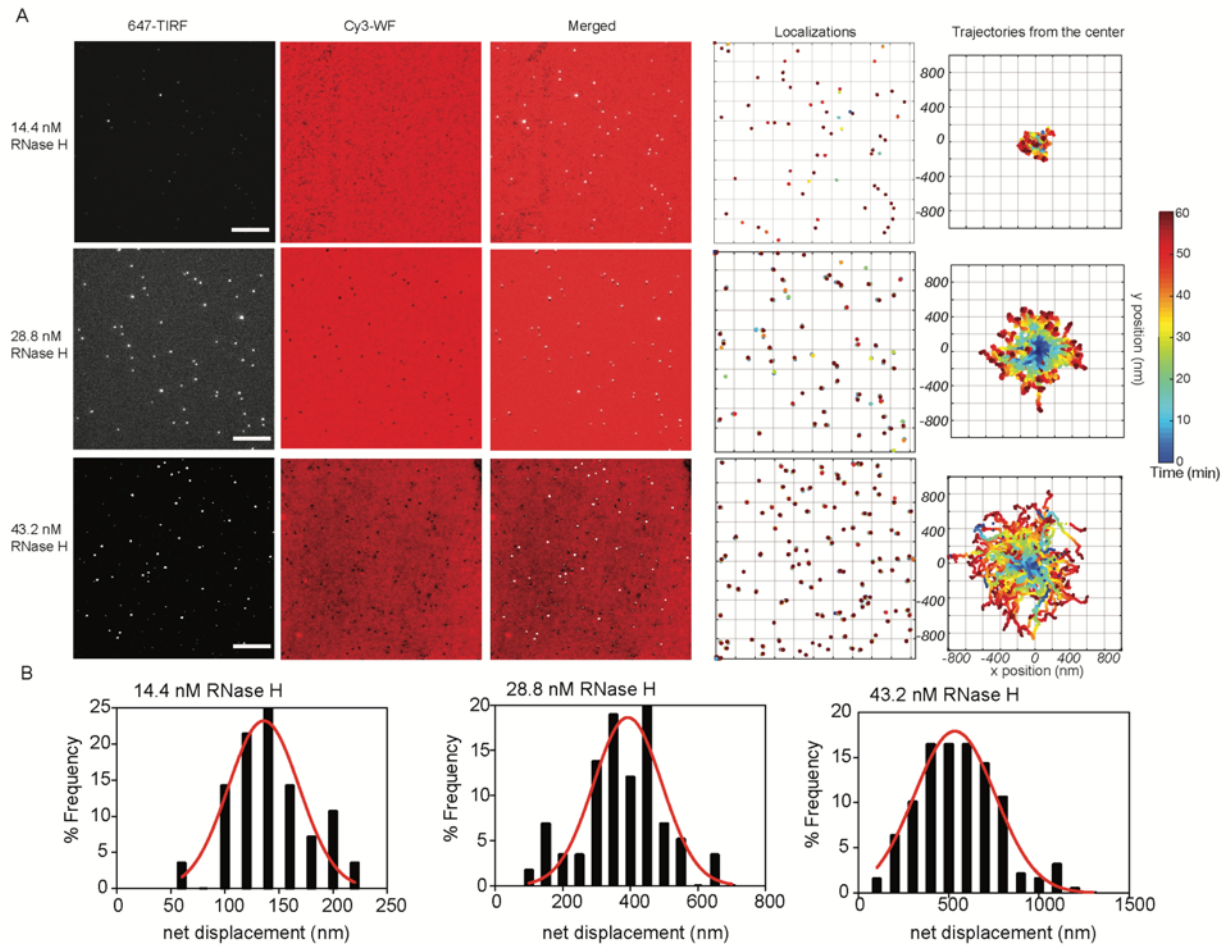


16HB 8



Supplementary Figure 9. Analyses of individual trajectories of a positive control. (A) Representative TIRF 647, Cy3 and overlay image taken from a time lapse video of motor translocation. The white boxes indicate 8 motors that are tracked in B and C. Scale bars are 10 μm . **(B)** Localization of AF647 trajectories from time lapse shown in A. **(C)** Analyses of eight individual trajectories. For each 16HB a merged image of AF647 16HB motor and Cy3 fuel is shown. Next, the smoothed trajectory of AF647 localizations is shown with a line demonstrating the net displacement calculation. To the right is a plot of total displacement (Euclidean distance of between each two points). The final point at ($t=60$) provided the total displacement for a given motor. The histogram displays the measured instantaneous velocities of each motor. Average velocity is calculated by fitting a gaussian curve to this histogram. Lastly, a plot showing the dependence of mean square displacement vs time was used to determine the alpha value for each motor. Each point in the plot is the average of mean square displacements of all the lag times corresponding to a given time. The alpha value is equal to the exponent of this power dependence. Scale bars are 1 μm .

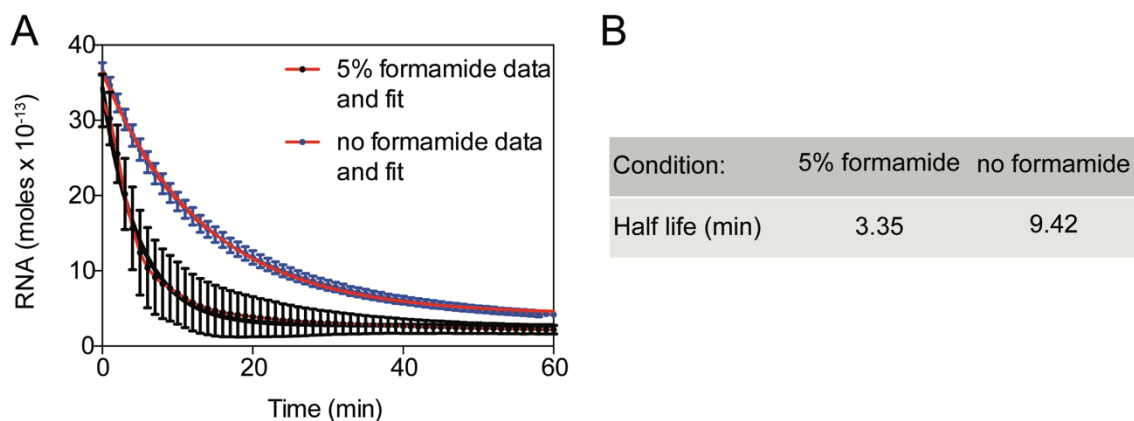
7. Effect of enzyme concentration on 16HB motor



Supplementary Figure 10. Raw data for effect of enzyme concentration on 16HB performance. (A) Representative TIRF 647, Cy3 and overlay image taken from a time lapse video and fitted 647 localizations along with all trajectories obtained from these samples. Scale bars are 10 μm . (B) Histogram of net displacements as a function of RNase H concentration ($n = 27, 58$ and 173 for $14.4, 28.8$ and 43.2 nM respectively).

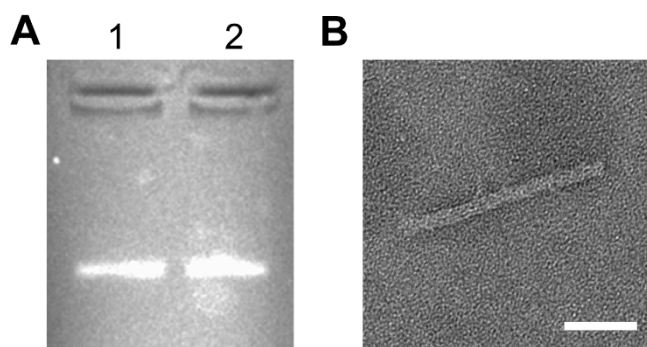
8. Kinetic measurements of RNase H activity

The RNA monolayer was hybridized to a complementary DNA strand overnight (“Thiolated DNA leg” in Table S2). The hybridized surface was washed with 1x RNase H buffer 3 times. The microfluidic chamber was placed on the microscope and a solution containing 28.8 nM RNase H was added to the surface in the presence and absence of formamide. Fluorescence decay was measured as a function of time. The absolute number of RNA molecules (y-axis) was calculated by multiplying the area of micro-channel by the density of RNA that was obtained from the calibration curve and release measurements shown in Fig S4. Fluorescence decay due to photo bleaching was also measured and subtracted from the data. Half-life of the reaction was calculated by fitting to an exponential decay function.



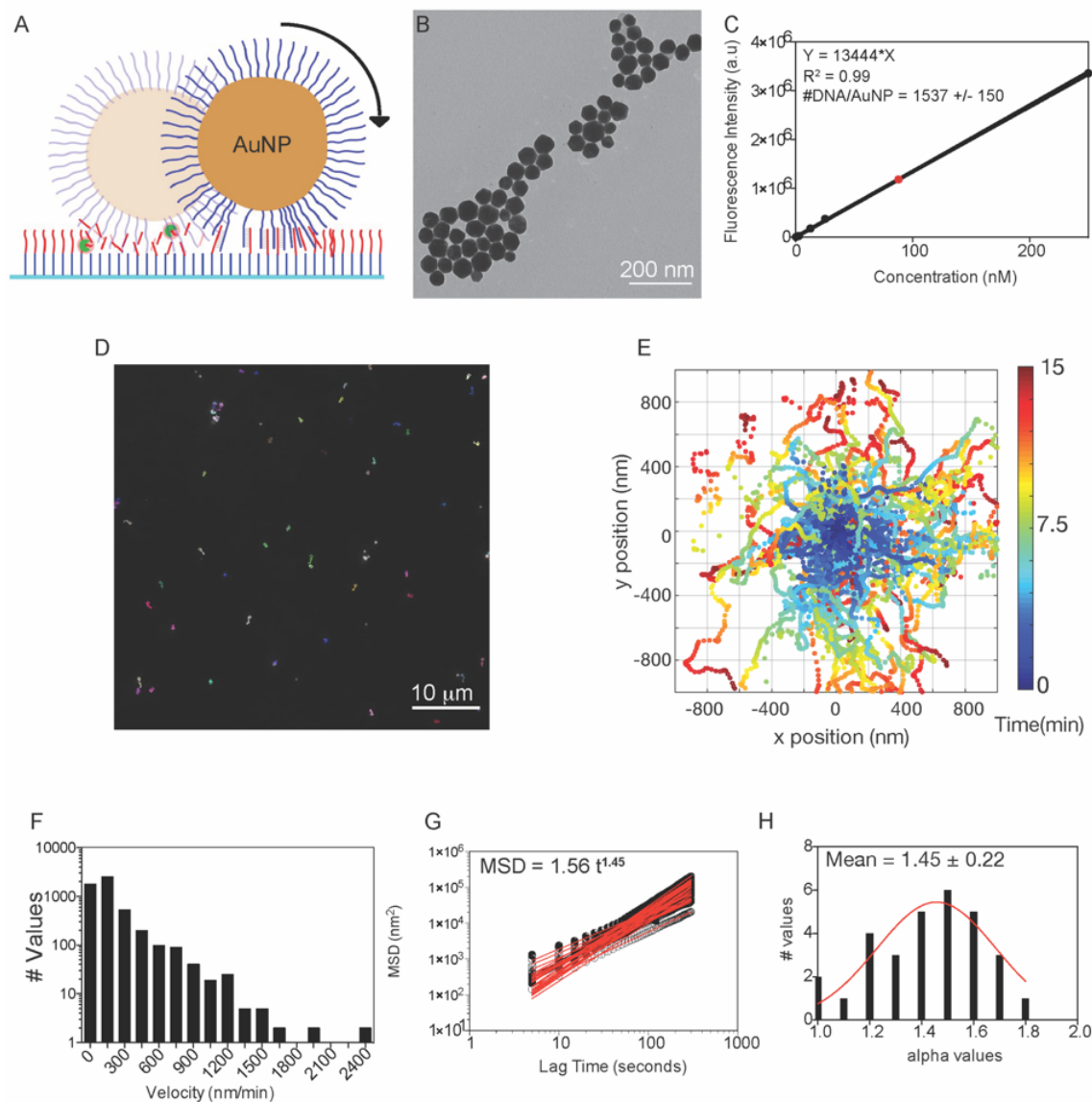
Supplementary Figure 11. Kinetic analyses of RNase H activity on the surface. (A)

Representative kinetic plots showing RNase hydrolysis of surface immobilized RNA hybridized to complementary DNA strand. The error bars represent the standard deviation in the average fluorescence intensity of region of interest imaged on the surface. The absolute number of RNA molecules (y-axis) was calculated by multiplying the area of micro-channel by the density of RNA per μm^2 that was obtained from the calibration curve and release measurements shown in Fig S4. (B) A table summarizing the results of the kinetic measurements.



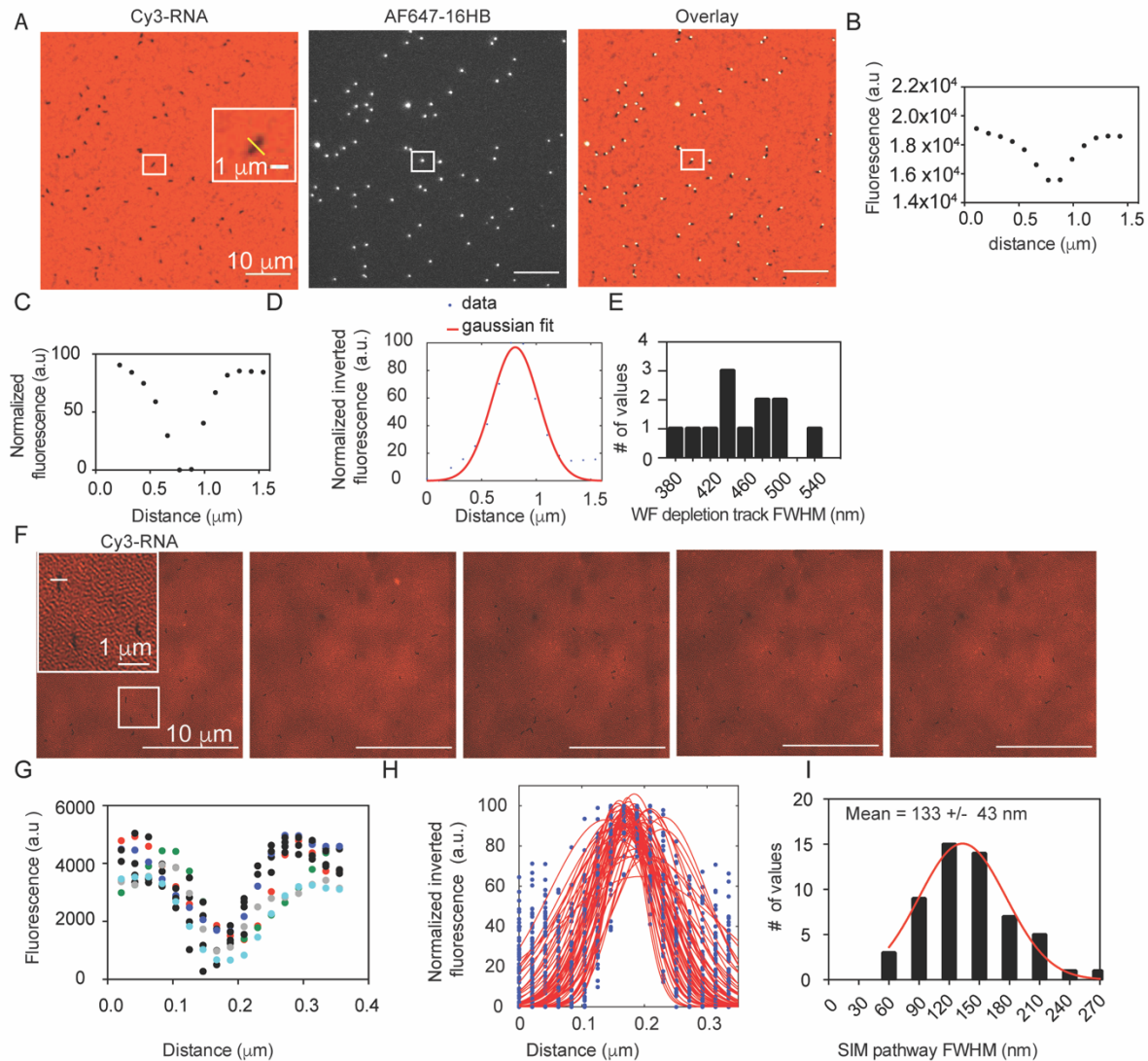
Supplementary Figure 12. Stability of 16HB in assay buffer. Stability of 16HB in RNase H solution was analyzed using (A) Agarose gel electrophoresis; 1: 16HB in 1xTE+10mM Mg²⁺, 2: 16HB in RNase H buffer (B)TEM image of 16HB in RNase H buffer showing intact structure after 12 hour incubation in RNase H buffer.

9. Synthesis of spherical motors

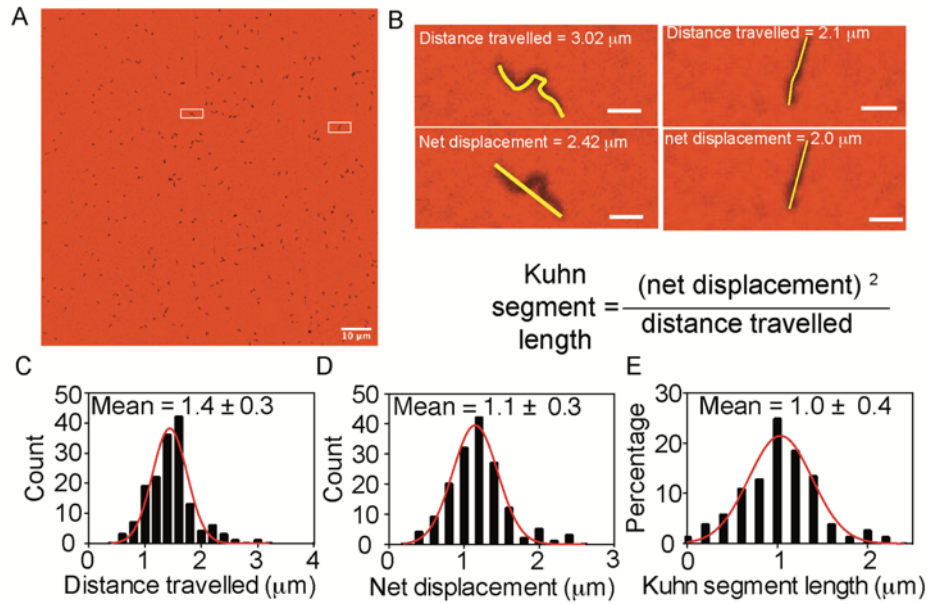


Supplementary Figure 13. Isotropic spherical motors move in a self-avoiding but not ballistic manner (A) Schematic of gold nanoparticle motor. (B) TEM image of gold nanoparticles. Scale bar is 200 nm. (C) Calibration curve used to determine DNA density on AuNP. The red dot shows the signal for a solution of 0.04 nM nanoparticles. (D) Motor trajectories overlaid onto the RICM image to show particle motion. Each trajectory was assigned a different color and was analyzed from a 15 min time lapse video. (E) Ensemble of trajectories of spherical motors overlaid starting at the origin of the plot $n = 42$ nanoparticles. $n = 30$ met the criteria for further analyses. (F) Instantaneous velocity histogram of spherical motors $n = 5368$ from $n = 30$ motors. (G) MSD vs time plots obtained from single particle tracking $n = 30$. Each point represents the average of all the lag times corresponding to a time t . Each red line represents the log-log fit to the data for individual trajectories. (H) Histogram of alpha values for spherical motors displaying an average alpha value of 1.45 ± 0.22 .

10. Analyses of width and length of depleted tracks

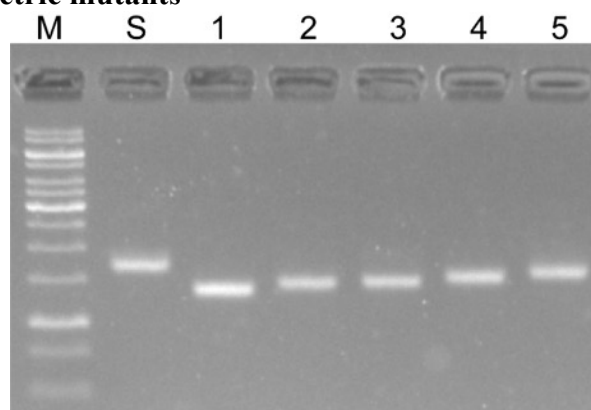


Supplementary Figure 14. Analyses of widths of Cy3 depletion tracks using WF and SIM microscopy. (A) Representative Cy3, AF647 and overlay image. (B) Linescan of the region highlighted. (C) Normalized fluorescence intensity and (D) an inverted fluorescence intensity. The data in (D) was fit to a Gaussian and the FWHM was used to infer the width of the track. (E) Histogram of depletion track width determined using WF imaging ($n = 12$). FWHM were calculated by fitting the normalized inverted fluorescence values to $f(x) = a_1 * \exp(-((x-b_1)/c_1)^2)$ and the full width at half maximum is defined as $FWHM = (c_1/1.4142) * 2.355 * 1000$. (F) Representative SIM images of depletion tracks. Scale bar is 10 microns. The white line represents an example location of where depletion track width analysis was performed. (G) representative linescans of individual tracks. The linescans had width of 10 pixels. (H) Normalized intensity values were plotted in blue while red shows the Gaussian fit to the inverted fluorescence linescans. (I) Histogram of FWHMs of 56 tracks using SIM. FWHM are calculated by fitting the normalized inverted fluorescence values to $f(x) = a_1 * \exp(-((x-b_1)/c_1)^2)$ then the full width at half maximum is defined as $FWHM = (f.c_1/1.4142) * 2.355 * 1000$.



Supplementary Figure 15. WF fluorescence analyses of depletion tracks. (A) Representative Cy3 image showing 16HB motor depletion tracks. (B) Zoom in on two trajectories and calculation of distance travelled and net displacement from Cy3 depletion. Scale bars are 1 μm . Histogram of distance travelled (C), net displacement (D), and Kuhn segment length (E) obtained from analysis of $n = 158$ depletion tracks obtained from three different experiments.

11. Generation of geometric mutants



Supplementary Figure 16. Agarose gel electrophoresis of 16HB-geometric mutants.

Mobility of 16HB decreases with increasing number of motor strands. M: 1kB DNA Ladder, S: p7560 scaffold strand, 1: 1-36, 2: 2c-36, 3: 2t-36, 4: 3-36, 5: 4-36

12. Modelling of 16HB motors

Model description: To develop a better understanding of the mechanism of our DNA origami motors, we developed a simple chemomechanical simulation method. In this simulation method, a motor is simulated translocating along a one-dimensional track with N “footholds” through either a rolling or walking mechanism (fig S17a and b). For the rolling mechanism, the simulated origami motor is similar to our 4-36 structure and has four “faces”, each of which can interact with every fourth foothold. For example, if $N = 12$ then face 1 interacts with footholds 1, 5, and 9, face 2 interacts with footholds 2, 6, and 10, face three interacts with footholds 3, 7, and 11, and face four interacts with footholds 4, 8, and 12. For the walking mechanism, the origami motor is similar to our 1-36 structure and, as such, only has one face that interacts with all footholds. At standard conditions, each face has 36 DNA legs and each foothold has 24 RNA fuel strands. This RNA fuel strand quantity was selected to reflect the 2/3 ratio of RNA fuel surface density (20,000 strands/ μm^2) to DNA feet density ($\frac{36}{0.120 \mu\text{m} * 0.01 \mu\text{m}} = 30,000$ strands/ μm^2). Interactions between legs and fuel strands are modeled in three steps: association, fuel cleavage, and dissociation (fig S17c). Below, we describe the kinetic models that we use to quantitatively model interactions between DNA origami faces and footholds. We then present the results of our simulation model and discuss the implications of these findings for our experimental work.

Reaction kinetics: Association occurs at a distance-dependent kinetic rate such that the origami motor legs interact preferentially with nearby footholds. For simplicity, we model the association rate as decreasing linearly from the parameter $k_{\text{on},0}$ to 0 as the distance between the origami body and the foothold (r) increases from zero to the cutoff distance, r_c (Figure S17 d). Beyond the cutoff distance, the association rate is zero. This is mathematically expressed as:

$$k_{\text{on}}(r) = \begin{cases} k_{\text{on},0} * \left(1 - \frac{r}{r_c}\right) & r < r_c \\ 0 & r \geq r_c \end{cases} \quad (1).$$

The overall rate of association between a face and foothold also depends on the amount of unpaired DNA legs at each face (D_u) and the amount of unpaired RNA fuel at the footholds (R_u). Once a DNA leg and RNA fuel strand hybridize, we assume that they cannot dehybridize until the RNA is cleaved by RNase H. As such, we model cleavage as occurring at a constant rate (k_{clvg}) that is related to the RNase H concentration. Following RNase H-mediated cleavage, the length of the duplex is substantially decreased (e.g. from 15 bp to 3 bp) and the off rate therefore increases from 0 to k_{off} . Because extended duplexes are subjected to tension, they will experience an increased off rate. As such, we also model k_{off} as increasing linearly with r (fig. S17 e):

$$k_{\text{off}}(r) = k_{\text{off},0} \left(1 + \frac{r}{r_c}\right) \quad (2)$$

While k_{off} is generally high when formamide concentration is high^[7], it also decreases with decreasing concentrations of formamide. In addition, burnt fuel strands – which we assume to retain short pairing regions a few nucleotides long – can interact with DNA legs. Because the kinetics of duplex formation are only weakly dependent on duplex length^[8], we simply use equation (1) to model the kinetics of association between consumed fuel and DNA legs. While legs exhibit higher overall affinity for fuel strands, their association with unpaired burnt fuel (B_u) can also have important effects on translocation behavior.

Mechanical relationships: At any given time, the position of the motor (x_M) is controlled by its adhesion with the footholds via a weighted average:

$$x_M = \frac{\sum_{i=1}^N ((R_{B,i} + B_{B,i}) * x_i)}{\sum_{i=1}^N (R_{B,i} + B_{B,i})} \quad (3)$$

Where $R_{B,i}$ is equivalent to the number of legs hybridized to fuel strands in the i^{th} foothold, $B_{B,i}$ is equivalent to the number of legs hybridized to burnt fuel strands in the i^{th} foothold, and x_i is the x-position of the i^{th} foothold. (Note that we use arbitrary units for distance and footholds are evenly spaced at one-unit intervals). In turn, the position of the origami motor dictates the association and dissociation kinetics; r , which influences k_{off} and k_{on} , is related to the position of the origami motor:

$$r_i = x_M - x_i \quad (4)$$

where x_i is the x-position of the i^{th} foothold and r_i is the distance between the motor and the i^{th} foothold.

Change equations: Now that the chemical and mechanical relationships of our system are defined, we define the differential equations that govern the time-dependence of the system. For each foothold, there are four distinct populations of RNA fuel strands: unbound RNA fuel (R_U), bound RNA fuel (R_B), unbound burnt fuel (B_U), and bound burnt fuel (B_B). Each of these populations is represented by a continuous variable. Each variable changes as a function of time due to interactions with the origami motor and, as such, has its own rate equation. In addition, each face of the origami motor has two populations of DNA legs: unbound DNA legs (D_U), and bound DNA legs (D_B). Each of these populations is also associated with a time-dependent variable and thus has its own governing equation. In total, there are $4N + 8$ equations for the rolling simulation and $4N + 2$ equations for the walking simulation. For the purposes of this simulation, we treat all variables as continuous variables that change smoothly as a function of time.

Assuming that association is a simple second-order process that depends linearly on both the amount of unpaired DNA feet and unpaired RNA fuel strands, the governing equation for the rate of change of unbound RNA fuel in the i^{th} foothold ($R_{U,i}$) is:

$$\frac{d(R_{U,i})}{dt} = -k_{\text{on}}(r_i) * R_{U,i} * D_{U,j} \quad (5)$$

where j is the index corresponding to the face that the i^{th} foothold pairs with ($j = 1$ for the walking mechanism, but j is $1 + \text{rem}(i - 1, 4)$ for the rolling mechanism, because each face can interact with every fourth foothold). In other words, the rate of change of unpaired RNA fuel is only determined by the rate of association with legs. The governing equation for the rate of change of bound RNA fuel in the i^{th} foothold ($R_{B,i}$) is:

$$\frac{d(R_{B,i})}{dt} = k_{\text{on}}(r_i) * R_{U,i} * D_{U,j} - k_{\text{clvg}} * R_{B,i} \quad (6)$$

where the first term reflects the association process and the second term reflects the RNase H-mediated cleavage process. The governing equation for the rate of change of bound burnt RNA fuel in the i^{th} foothold ($B_{B,i}$) is:

$$\frac{d(B_{B,i})}{dt} = k_{\text{clvg}} * R_{B,i} - k_{\text{off}}(r_i) * B_{B,i} + k_{\text{on}}(r_i) * B_{U,i} * D_{U,j} \quad (7)$$

where the first term reflects the RNase H-mediated cleavage process, the second term reflects dissociation of the burnt fuel from the leg, and the third term reflects re-hybridization between the

burnt fuel and DNA legs. The governing equation for the rate of change of unbound burnt RNA fuel in the i^{th} foothold ($B_{U,i}$) is:

$$\frac{d(B_{U,i})}{dt} = k_{\text{off}}(r_i) * B_{B,i} - k_{\text{on}}(r_i) * B_{U,i} * D_{U,j} \quad (8)$$

where the first term reflects dissociation of the burnt fuel from the leg, and the second term reflects re-hybridization between the burnt fuel and DNA legs. The governing equations for rate of change of unbound DNA leg strands on the j^{th} face of the origami motor ($D_{U,j}$) is:

$$\frac{d(D_{U,j})}{dt} = \sum_{i=1}^N k_{\text{off}}(r_i) * B_{B,i} - k_{\text{on}}(r_i) * (B_{U,i} + R_{U,i}) \quad (9)$$

for the walking mechanism, and

$$\frac{d(D_{U,j})}{dt} = \sum_{i=j,j+4,j+8,\dots}^N k_{\text{off}}(r_i) * B_{B,i} - k_{\text{on}}(r_i) * (B_{U,i} + R_{U,i}) \quad (10)$$

for the rolling mechanism. In both cases, the first term reflects dissociation of burnt fuel and DNA legs and the second term reflects association of DNA legs with RNA fuel and burnt fuel. Finally, we note that, because $D_{B,j} = 1 - D_{U,j}$, the governing equation for $D_{B,j}$ is simply:

$$\frac{d(D_{B,j})}{dt} = - \frac{d(D_{U,j})}{dt} \quad (11)$$

we also define the total polyvalency (P), as the total number of legs bound to the track:

$$P = \sum_{i=1}^N (B_{B,i} + R_{B,i}) \quad (12)$$

For initial conditions, we defined the motor as connected to footholds 1 and 2 at a polyvalency via twelve strands (which is 50%) for each foothold. In terms of the variables defined above, at $t = 0$ we define $R_{U,i} = R_{B,i} = 12$ for $i \leq 2$, $R_{B,i} = 0$ and $R_{U,i} = 24$ for $i > 2$, $B_{U,i} = B_{B,i} = 0$ for all i (denoting that no fuel is burnt). At $t = 0$, we also define also $D_{B,1} = 24$ (for the walking mechanism) or $D_{B,i} = 12$ for $i \leq 2$ and $D_{B,i} = 0$ for $i > 2$ (for the rolling mechanism). Accordingly, in both cases $P = 24$ and $x_M = 1.5$ when $t = 0$.

Simulation assessment metrics: For the purpose of this work, we are interested in understanding how kinetic parameters (e.g. k_{clvg} and $k_{\text{off},0}$, which can be experimentally tuned via RNase H concentration and formamide volume fraction, respectively) and geometric parameters (e.g. the number of legs and leg-presenting faces on the motor) can affect dynamic properties of the motor such as speed, processivity, and persistence. As such, it is important to determine robust methods with which to measure these emergent properties from these simulations.

A simulated motor can be either processive or non-processive. A processive motor must be able to, in the context of this simulation, translocate across arbitrarily large distances given enough time. A motor is non-processive if it either 1) detaches from the surface, which we define as happening when $P < 0.5$ (which rounds down to a polyvalency of zero) or 2) stalls due to association with burnt fuel in a manner that makes it incapable of transitioning to new footholds, even given infinite time.

To classify each simulated motor as processive or non-processive, we define a ‘‘processive motion cutoff distance’’, x_p , of $x_p = N + 1 - r_c$. We reasoned that, if the motor can traverse the track and

reach x_p , it would be within binding range of the $(N + 1)^{\text{th}}$ foothold (if the foothold existed). Under appropriate conditions, it is reasonable to assume that it would then be capable of crossing the $(N + 1)^{\text{th}}$ foothold and reaching the $(N + 2)^{\text{th}}$ foothold, and so on. In other words, if the motor can reach x_p , the motor can be expected to continue translocating indefinitely on a track of infinite length due to the deterministic nature of this simulation method. After each simulation timestep we check to make sure that $P \geq 0.5$ and that the motor is not moving backwards in the $-x$ direction. If either condition is violated before the motor reaches x_p , the simulation is terminated, and the motor is labeled non-processive at the tested condition. In addition, to save computational time we also check to see if the motor's speed has decreased below a small positive cutoff velocity of 10^{-6} min^{-1} . Such a low velocity very likely suggests that the motor has stalled and is asymptotically converging to a position that is smaller than x_p . Finally, in order to ensure computational tractability, we set a maximum simulation time (t_{max}) of $t_{\text{max}} = 60 \text{ min}^{-1}$. If the motor has not reach x_p within this time then, although it may technically be processive, it is labeled as non-processive because it is effectively too slow to be meaningfully benchmarked against experimental observations.

If a simulated motor is classified as processive we can characterize its speed and persistence. Note that due to the periodic nature of the track, the motor, if processive, will also exhibit periodic nature in its translocation. Specifically, the motor will exhibit dynamic steady-state behavior with a spatial periodicity that matches the 1-unit spacing of the footholds on the track. This dynamic steady-state behavior will not immediately be evident because the initial conditions (e.g. motor position and associations with the track) will likely not resemble the dynamic steady state behavior. As such, the simulation must be given sufficient time for the system to reach a dynamic steady-state. This can largely be accomplished by setting $N = 10$. Following the establishment of a dynamic steady state, a single "cycle" can be isolated and analyzed to fully understand the processive dynamic behavior of the motor at that condition. We extract this cycle by isolating the simulation output from when $(x_p - 1) \leq x_M < x_p$, which occurs over a time span τ . The motor's velocity (in units of min^{-1}) is equivalent to τ^{-1} . The motor's persistence, we argue, can be indirectly related to the average and minimum P over the course of this cycle because lower polyvalency will allow for an increased role of Brownian fluctuations.

Results: Using the mathematical relationships and assessments described above, we next set parameter values and ran representative simulations. For an initial test run, we tested the rolling mechanism with $r_c = 1.5$, $k_{\text{on},0} = 1 \text{ s}^{-1}$, $k_{\text{clvg}} = 3 \text{ s}^{-1}$, $N = 4$, and $k_{\text{off}} = 1 \text{ s}^{-1}$ or $k_{\text{off}} = 3 \text{ s}^{-1}$. Using this parameterization, we saw that, for $k_{\text{off}} = 3 \text{ s}^{-1}$, the motor was processive (Figure S17f). However, increasing the affinity of the legs for burnt fuel by decreasing k_{off} to 1 s^{-1} resulted in the motor becoming non-processive and stalling at $x_M = 2$ (Figure S17f).

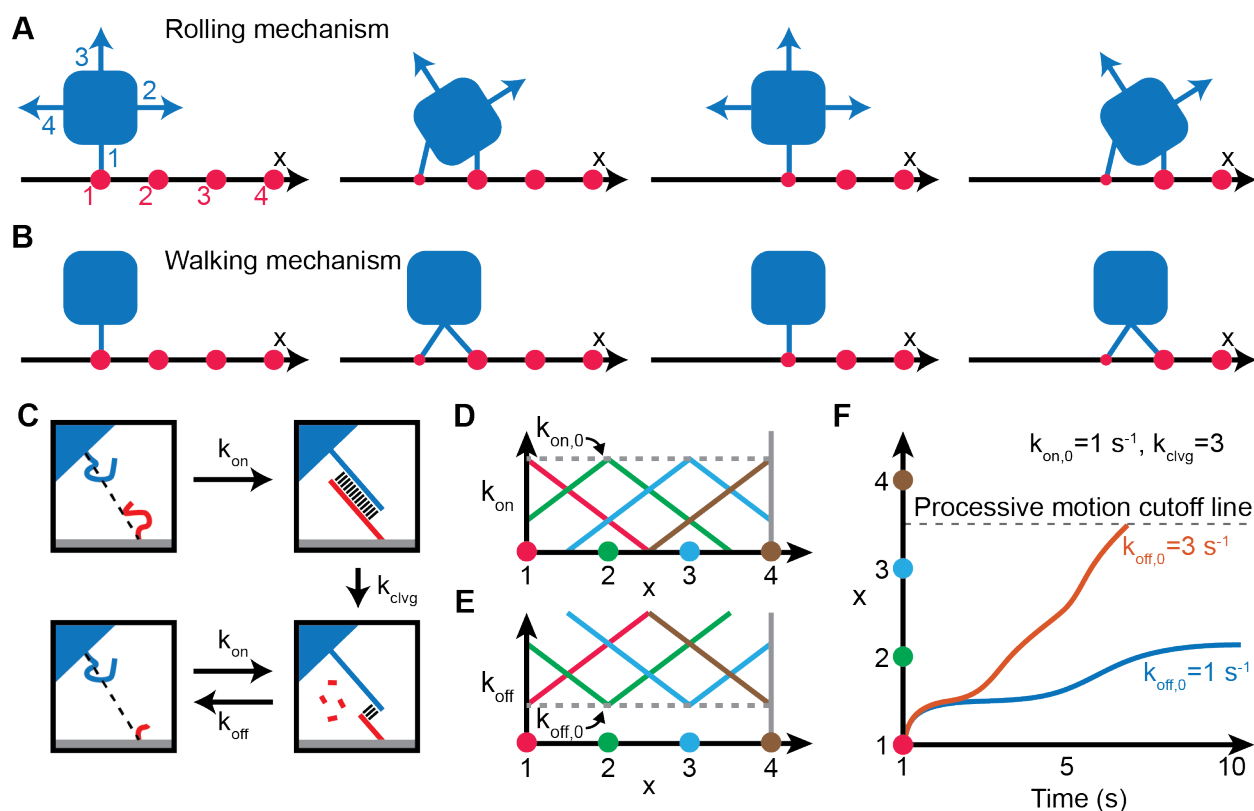
We next performed comparisons between the walking and rolling mechanisms. For this comparison, we considered the distinction between the two mechanisms. We increase N to ten footholds to allow for convergence to a dynamic steady state. Beyond differences in change equations between the two mechanisms, we also considered differences in their kinetic behavior. Specifically, we note that thermal (Brownian) fluctuations of the body of the motor will likely result in a greater binding range for the rolling mechanism than the walking mechanism. In other words, if a motor is bound to foothold 1, Brownian fluctuations will allow the motor to "swivel" around foothold 1 without substantially extending the legs bound to foothold 1. This swiveling

will allow the motor to diffuse closer to and farther from foothold 2. In contrast, for the walking mechanism swiveling will make no difference to association kinetics. As such, we expect that the association kinetics for the rolling and walking mechanisms will be slightly different due to increased mobility of the forward-facing face in the rolling mechanism. To account for this, we used slightly different association kinetic parameters for the two mechanisms; we set $k_{\text{on},0} = 1 \text{ min}^{-1}$ and $r_c = 1.75$ for walking, and $k_{\text{on},0} = 0.875 \text{ min}^{-1}$ and $r_c = 2$ for rolling. Note that these slight parameter differences balance out such that the area under the k_{on} vs. r curve is the same for the two conditions. Setting $k_{\text{clvg}} = k_{\text{off}} = 1 \text{ min}^{-1}$ resulted in stalling for both mechanisms (not shown), but setting $k_{\text{clvg}} = k_{\text{off}} = 5 \text{ min}^{-1}$ resulted in processive motion for both mechanisms (Figure S18).

For the rolling mechanism, periodic association between the track and each of the four faces was indeed observed, and within ~five minutes of simulation time an apparent dynamic steady-state was established (Figure S18b). Similarly, the walking mechanism showed the same periodicity and rapidly-developed dynamic steady state when footholds were sorted into four groups (Figure 18a). Comparison of the x_M vs. t curves (Figure S18c) of the two conditions reveals that the rolling mechanism is similar to the walking mechanism, but slightly (~15%) faster under these conditions. Additionally, the motor speed and average polyvalency vs. time curves are qualitatively different between the two mechanisms; while the speed oscillates from $\sim 0.75 \text{ min}^{-1}$ to $\sim 1 \text{ min}^{-1}$ for the rolling motor, velocity oscillates much more substantially from $\sim 0.3 \text{ min}^{-1}$ to $\sim 1.2 \text{ min}^{-1}$ for the walking motor. Similarly, the total polyvalency of the motor is both higher (on average) and more stable for the rolling mechanism than the walking mechanism. This simulation method is deterministic in nature and, as such, does not account for the effect of noise. However, in experimental scenarios thermal fluctuations are expected to play a substantial role in the motion of origami motors. Because our simulated walking motors exhibit velocity and polyvalency values that undergo more substantial oscillations and lower minimums than rolling motors, we speculate that walking motors are more sensitive to noise (e.g. thermal fluctuations) than rolling motors. The expected effect of this heightened sensitivity to noise is a decrease in the observed path persistence of origami motor motion; if the optimal mode of translocation involves movement perpendicular to the long axis of the motor (which is highly persistent), then noise will increase the frequency of non-optimal modes of translocation (e.g. turning, flipping, etc.), thus decreasing the overall persistence. This finding helps to explain why motors with geometries that promote rolling (e.g. the 4-36 structure) generally exhibit higher persistence than motors that are less well suited towards rolling and better suited towards walking (e.g. the 1-36 structure).

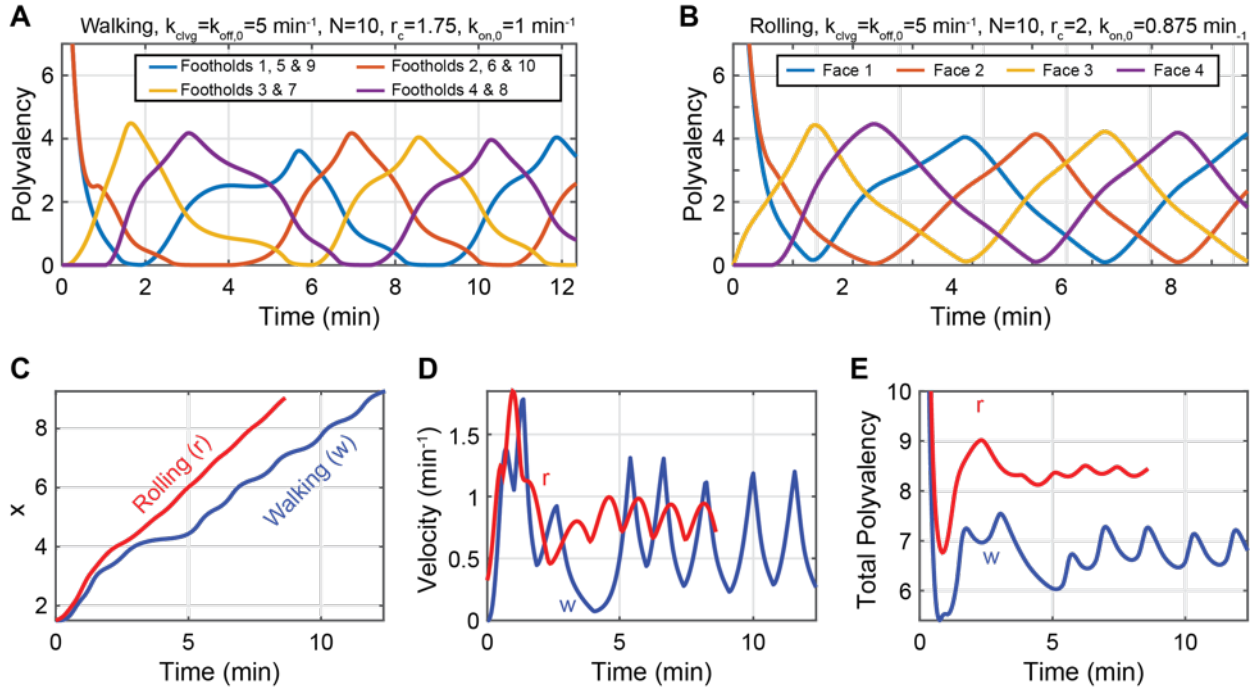
We next ran simulations at a representative set of combinations of k_{clvg} and $k_{\text{off},0}$ parameters ranging from 0.1 min^{-1} to $1,000 \text{ min}^{-1}$ to understand how the two parameters (which can be experimentally tuned by changing the RNase H concentration and formamide volume fraction, respectively) affect the observed type of motion. For these simulations, we used parameters described above: $k_{\text{on},0} = 1 \text{ min}^{-1}$ and $r_c = 1.75$ for walking, and $k_{\text{on},0} = 0.875 \text{ min}^{-1}$ and $r_c = 2$ for rolling, $N = 10$, and $t_{\text{max}} = 60 \text{ min}^{-1}$. We classified each condition as exhibiting persistent motion, detachment, or stalling as described above. Our results are shown in phase planes in Fig. S19. Both mechanisms exhibit all three types of behaviors in a manner that depends on the quantitative k_{clvg} and $k_{\text{off},0}$ values. Strikingly, the rolling mechanism possesses a significant region on the phase plane that corresponds to processive motion that is not processive for the

walking mechanism. We refer to this region as the “obligatory rolling” region. Our observation that at low formamide only the 4-36 structure exhibits motion, while all structures exhibit motion at high formamide, is consistent with this finding; it is possible that increasing the volume fraction of formamide increased $k_{\text{off},0}$ in a manner that switched the origami motor from an “obligate rolling” phenotype to a mixed rolling-and-walking phenotype. We have annotated the phase diagram in Figure S19c to denote this expected shift. We note that the velocities of the two mechanisms are highly similar, with only a $\sim 15\%$ difference between the two at high k_{clvg} . In addition to these trends, we also generally see behavior that is consistent with our experimental findings. For example, increasing k_{clvg} increases velocity monotonically until the point of detachment (Figure. S19d). This is consistent with the finding that increasing RNase H increases velocity. Increasing the off rate increases the velocity in an asymptotic function, and at very high $k_{\text{off},0}$ the effect of k_{off} dissipates (Figure S19e). This finding is consistent with the observed increase in velocity with increasing formamide volume fraction. Finally, decreasing the number of feet results in a corresponding decrease in the velocity in a linear manner (Figure S19f), as is also consistent with experimental observations.

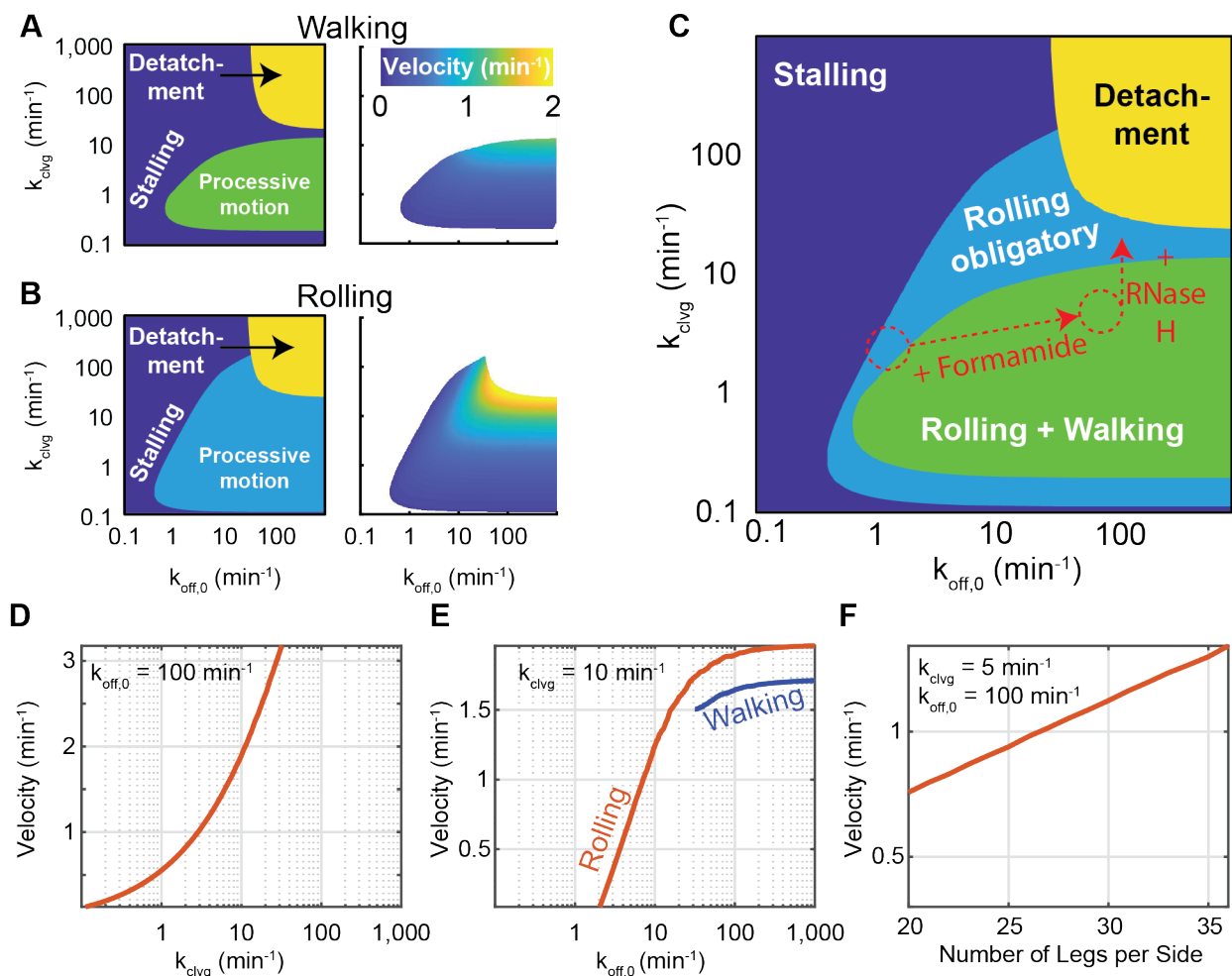


Supplementary Figure 17. Schematic depiction of chemomechanical simulation method and representative results. Cartoon depiction of simulation method for (A) rolling and (B) walking mechanisms. For each mechanism a single origami motor (blue) is simulated with a track that contains four footholds (red dots). The motor then rolls or walks according to association with, destruction of, and detachment from the footholds, and the position of the motor is determined by the degree of binding to each foothold. (C) Depiction of kinetic mechanism used to simulate

origami translocation. DNA legs can associate with RNA fuel with rate k_{on} and the hybridized fuel strands can be degraded with rate k_{clvg} . The degraded fuel is then assumed to retain some small affinity for the DNA legs and dissociates with rate k_{off} . DNA legs can also reversibly pair with degraded fuel. This minimal mechanism allows for the characterization of the effects of specific DNA-RNA interactions, as well as nonspecific interactions with burnt fuel (which resemble friction). Kinetic rate constants for **(D)** association and **(E)** dissociation of the origami motor with each of the four target sites as function of end-to-end distance. While fuel sites are all shown as red dots in **a** and **b**, they are shown in four different colors in **(D)** and **(E)** and the color of each curve denotes correspondence with the fuel site of the same color. These values decrease and increase, respectively, with increasing distances, reflecting a chemomechanical coupling wherein mechanics influence chemical kinetics. In turn, chemical kinetics influences mechanics because the motors position is controlled by adhesion to fuel. **(F)** Representative distance vs. time curves for sample simulations run with $k_{\text{on},0} = 1 \text{ s}^{-1}$, $k_{\text{clvg}} = 3 \text{ s}^{-1}$, and $k_{\text{off}} = 1 \text{ s}^{-1}$ or $k_{\text{off}} = 3 \text{ s}^{-1}$. The former ($k_{\text{off}} = 1 \text{ s}^{-1}$) stalls at $x=2$, while the latter ($k_{\text{off}} = 3 \text{ s}^{-1}$) continues moving beyond $x=3.5$, at which point we define the motion as “processive” because the motor would bind to a fifth site and continue moving forward if the simulation were to continue. Color-coded target sites are displayed on the y-axis for reference.

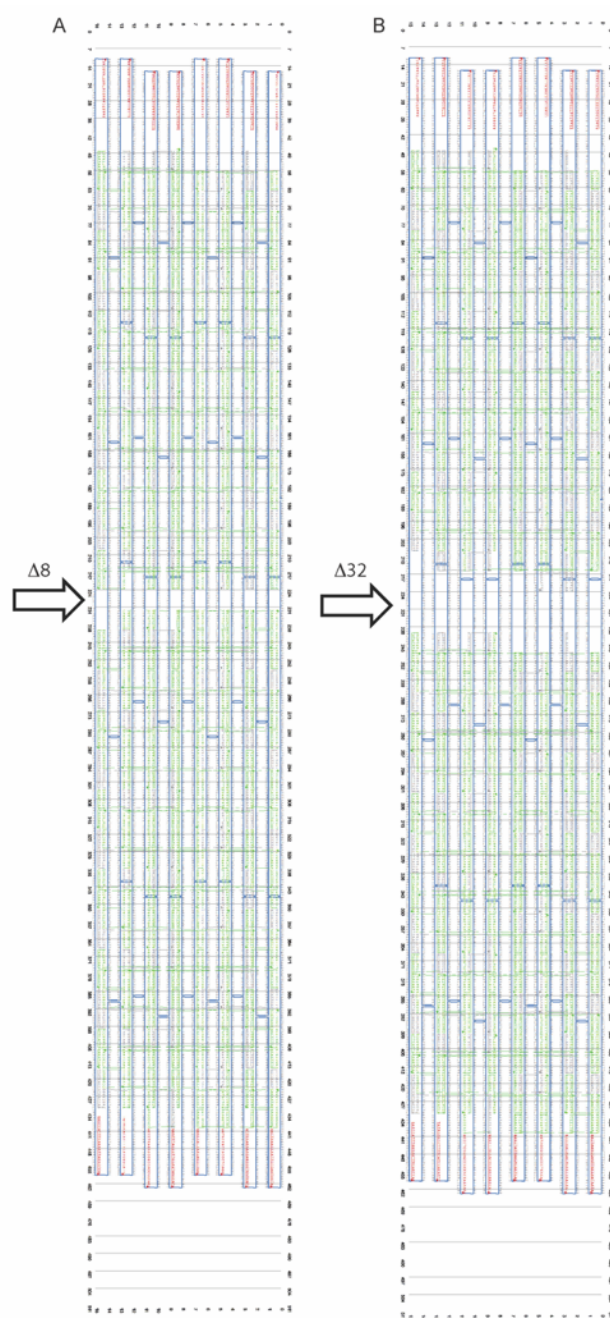


Supplementary Figure 18. Representative results comparing the rolling and walking mechanisms. (A) Polyvalency of foothold groups (where every fourth foothold is in the same group) as a function of time with the parameters shown for the walking mechanism. Each of the four curves has a distinct color corresponding to one of the four groups. (B) Same as (A), but with the rolling mechanism. The foothold groups were selected such that, for the rolling mechanism, rolling group 1 pairs with legs on face 1, 2 pairs with legs on face 2, etc. and the groups are the same between the two mechanisms. In both plots, periodic behavior can be observed. (C) Displacement vs. time for the rolling (r) and walking (w) simulations conditions. (D) Velocity vs. time for the two simulations. (E) Total polyvalency vs. time for the two simulations. A more detailed discussion of these results is brought in supplementary text above.

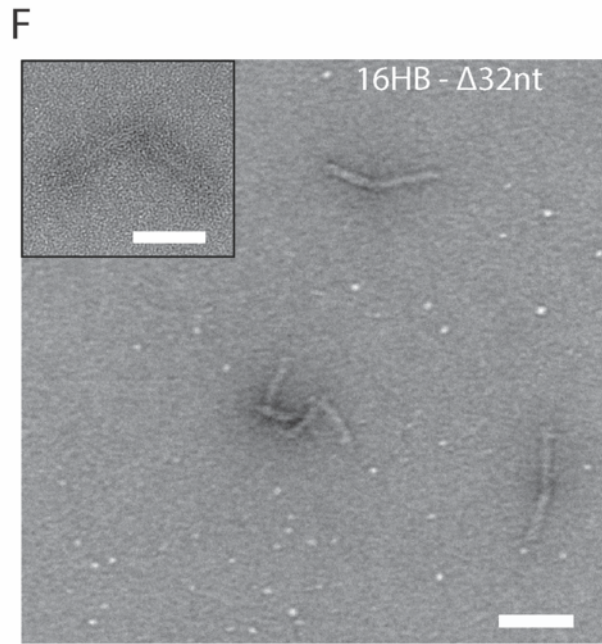
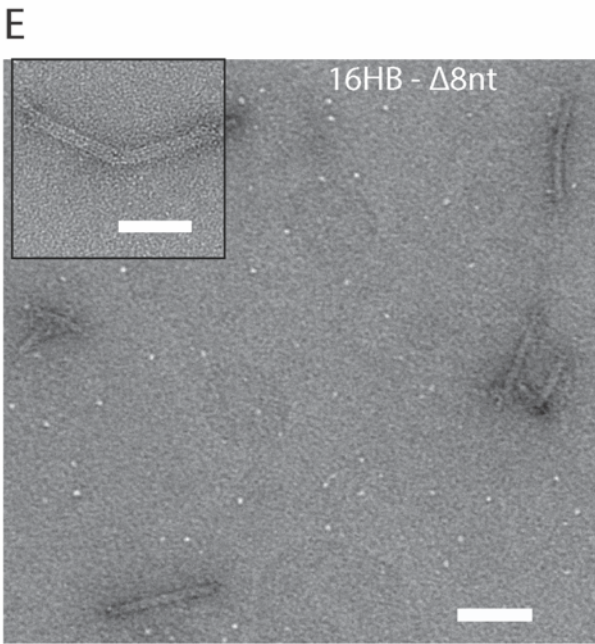
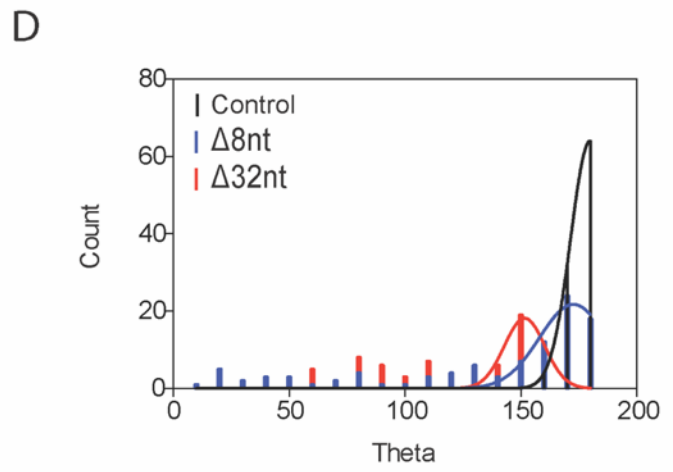
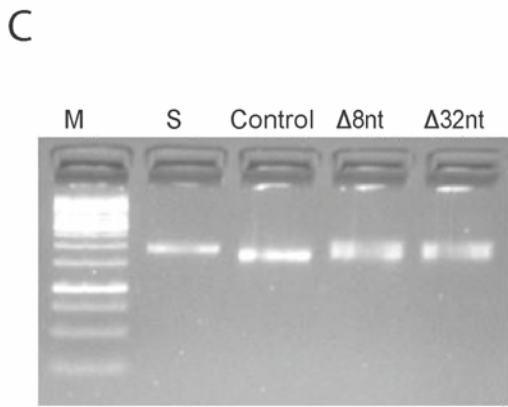
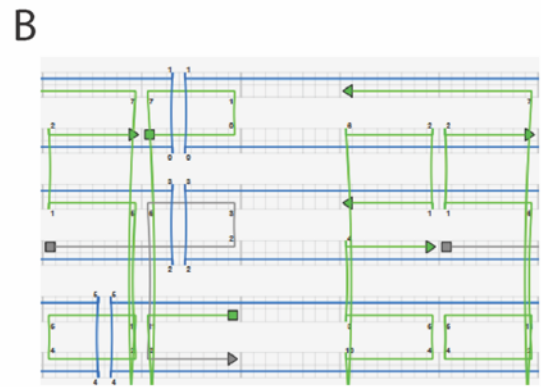
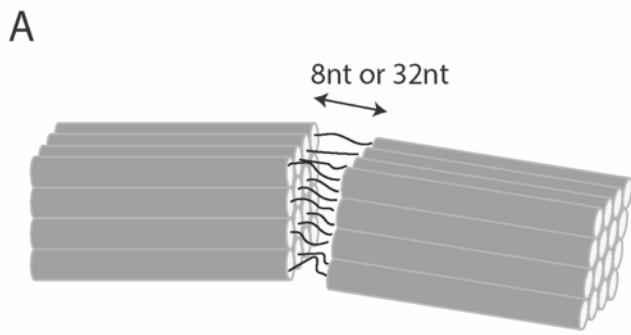


Supplementary Figure 19. Simulation-based comparison of rolling and walking mechanisms. Phase diagram (left) and velocity plot (right) showing the type of motion exhibited and calculated velocity obtained from simulations with $k_{\text{off},0}$ and k_{clvg} spanning five orders of magnitudes from 0.1 s^{-1} to $1,000 \text{ s}^{-1}$ for the (A) walking and (B) rolling mechanisms. All simulations were performed with $k_{\text{on},0}=1 \text{ s}^{-1}$. A given simulation was considered processive if the position reached the “processive motion cutoff line” shown in fig. S17f. A given simulation was considered “detached” if the overall polyvalency of the walker reduced to below 0.5 (which rounds to zero tethers). A simulation was considered “stalled” if the motor exhibited backward motion at any time. (C) Mixed phase diagram showing the expected rolling behavior of a DNA origami roller as a function of $k_{\text{off},0}$ and k_{clvg} . At low k_{off} , the motors stall. Increasing k_{off} (akin to increasing the amount of formamide in the rolling buffer) first results in a “obligatory rolling” phase, in which motors can move via the rolling mechanism but not the walking mechanism. Further increasing k_{off} , and with sufficiently high k_{clvg} , results in a mixed rolling / walking phase in which the rolling and walking mechanisms exhibit similar velocities. (D) Velocity vs. k_{clvg} with $k_{\text{off},0} = 100 \text{ min}^{-1}$, which resembles the situation where formamide is present in a high-volume fraction, for the rolling mechanism. (E) Velocity vs. $k_{\text{off},0}$ where $k_{\text{clvg}} = 10 \text{ min}^{-1}$ for both the rolling and walking mechanisms. (F) Velocity vs. the number of legs per side when $k_{\text{clvg}} = 5 \text{ min}^{-1}$ and $k_{\text{off},0} = \text{min}^{-1}$ for the rolling mechanism.

13. Tuning the flexibility of 16HB motors

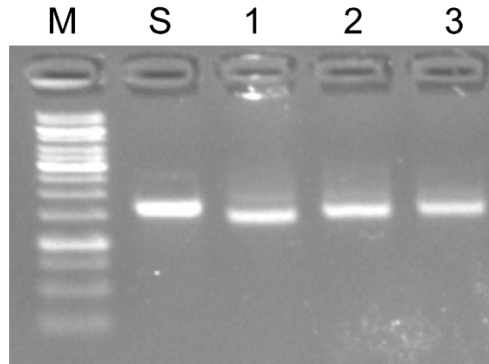


Supplementary Figure 20. caDNAno design files of flexible 16HB motors. Green staples contain RNA-binding domains and red staples are cargo binding strands. (A) $\Delta 8$ nt and (B) $\Delta 32$ nt designs. Arrows indicate the location of the deleted strands used to generate each flexible mutant.

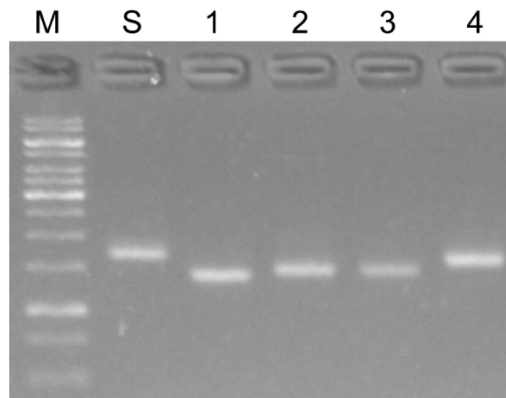


Supplementary Figure 21. Characterization of flexible 16HBs. (A) Schematic design of flexible 16HB motors. Select staple strands were removed to produce ssDNA regions of different lengths (8 nucleotides and 32 nucleotides named $\Delta 8nt$ and $\Delta 32nt$) to introduce flexibility to the rod structure. (B) Region of caDNAno design file for $\Delta 8nt$ showing removal of select staple strands to produce 8nt long ssDNA region of scaffold strand. Additional staple strands were then removed to produce a 32nt ssDNA scaffold region. Full caDNAno files of both flexible designs can be found in Figure S20. (C) Mobility of flexible mutants of 16HB. M: 1kB DNA Ladder S: p7560 Scaffold Strand. Control: Rigid 16HB. $\Delta 8nt$ and $\Delta 32nt$ are the flexible mutants. (D) Histogram of thetas (angle between two ends of 16HBs) obtained from TEM images similar to ones shown in (E) ($\Delta 8nt$) and (F) ($\Delta 32nt$) and Fig.S2 (n = 100,100 and 89 for control, $\Delta 8$ and $\Delta 32$).

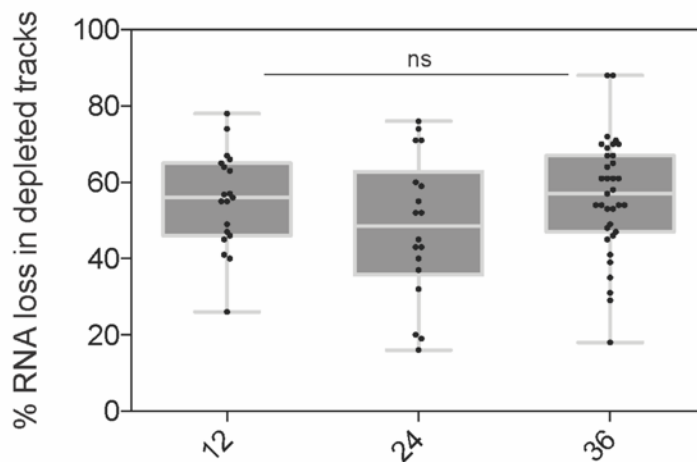
14. Generation and analyses of polyvalency/density mutants



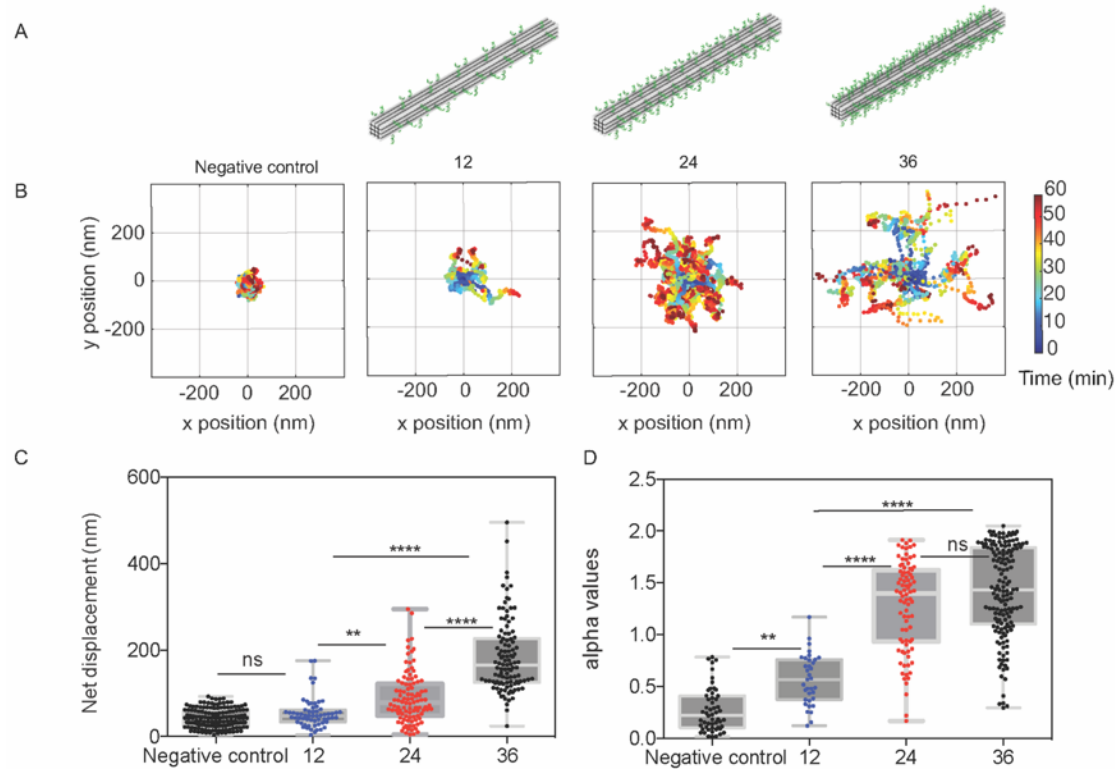
Supplementary Figure 22. Agarose gel electrophoresis of 16HB-density mutants. Mobility of 16HB decreases with increasing number of DNA legs. M: 1kB DNA Ladder, S: p7560 Scaffold Strand, 1: 4-12, 2: 4-24, 3: 4-36



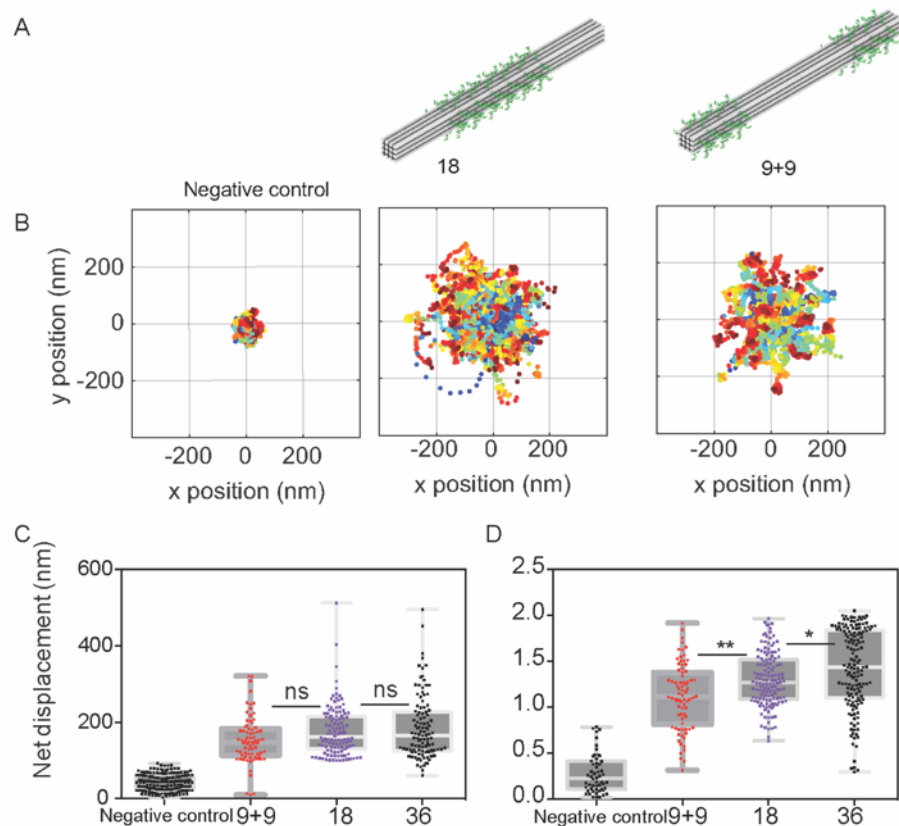
Supplementary Figure 23. Agarose gel electrophoresis of 16HB-polyvalency mutants. Mobility of 16HB decreases with increasing number of DNA legs. M: 1kB DNA Ladder, S: p7560 Scaffold Strand, 1: 16HB4-9, 2: 16HB4-9/9, 3: 16HB4-18, 4: 16HB4-36



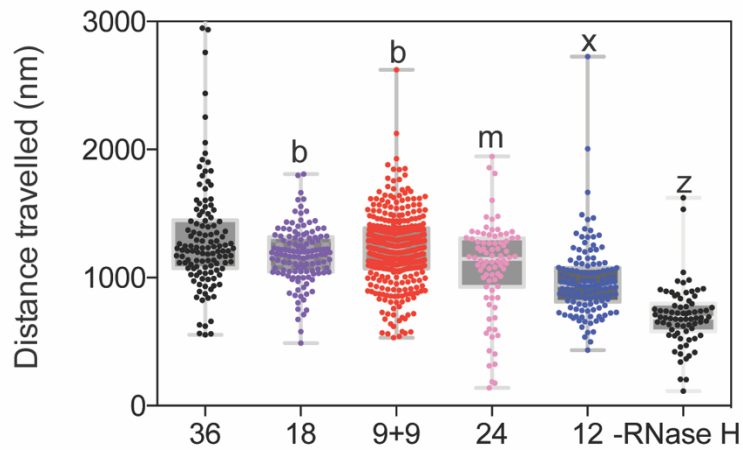
Supplementary Figure 24. Comparison of percentage of RNA lost in depletion tracks of 12, 24 and 36 16HB motors. A plot of fraction of RNA loss (%) in depletion tracks as a function of number of DNA legs per each face. Percent RNA loss in depleted tracks was calculated similar to Figure S6. $n = 19, 18$ and 35 for 12, 24 and 36 respectively obtained from two independent experiments.



Supplementary Figure 25. DNA leg density increases net displacement in higher stringency conditions withholding formamide. (A) Schematic design of 16HB library with different densities of DNA named with the number of legs 12, 24 and 36. Varying number of legs are spread out to keep chassis length constant hence changing surface density. (B) Trajectories from a representative experiment is plotted below each structure. The structures with 12 legs on each side are stalled in no formamide conditions. (C) Lower density of DNA legs results in diminished velocities and hence lower net displacements. (D) Plot of alpha values showing that motors with 24 and 36 DNA legs per face move in a ballistic manner $n = 54, 45, 88$ and 152 for negative control, 12, 24 and 36 respectively from 3 independent experiments. **, **** and ns represent $p < 0.01$, $p < 0.0001$ and not significantly different, respectively. Buffer contains 3 mM Mg^{2+} , 1 mM DTT , and 28.8 nM RNase H .



Supplementary Figure 26. DNA leg density dictates motor speed when withholding formamide (A) Schematic representation of 16HBs with 18 and 9+9 strands on each side. (B) Trajectories from representative experiments. (C) Comparison of net displacement of different structure without formamide. (D) Comparison of alpha values of different structures without formamide demonstrates a diminished alpha value for 9+9 compared to 18 and 36. Each dot represents a single motor, box represents 95% CI with median, and the bars represent the min and max. $n = 54, 78, 138$ and 152 for negative control, 9+9, 18 and 36 respectively generated from 3 different experiments (9+9 is two independent experiments). *, ** and ns demonstrate $p < 0.1$, $p < 0.01$ and not significantly different, respectively. Buffer contains 3 mM Mg^{2+} , 1 mM DTT, and 28.8 nM RNase H.



Supplementary Figure 27. Comparison of total displacement for 16HB with differing DNA leg density and distribution. Each dot represents a single motor, box represents 95% CI with median, and the bars represent the min and max. b, m, x indicate $p < 0.1$, $p < 0.01$ and $p < 0.0001$ respectively, in comparison to the 36. $n = 173, 116, 214, 55,$ and 98 for 36, 18, 9+9, 24, 12 and -RNase H, respectively.

15. Comparison of 16HB with other nanoscale motors

Supplementary Table 1. Comparison of 16HB DNA motor with other nanoscale motors.

	16HB Origami motor (<i>this work</i>)	Uni-pedal and bi-pedal BBR DNA walkers ^[9]	Polyvalent BBR DNA walkers ^[10]	Biological motors ^[11]
Step size ^[a]	~10 nm	~5-10 nm	~5-10 nm	~10 nm (kinesin ~8 nm)
Processivity ^[b]	Processive (100s of steps)	Limited	Limited (<100 steps demonstrated)	Processive (100s-1000s of steps)
Directionality ^[c]	Intrinsically Unidirectional	Track-guided	Track-guided	Track-guided
Speed ^[d]	20-100 nm/min	1-10 nm/min	1-10 nm/min ^[e]	~10 μm/min
Distances travelled	μm scale	nm scale	nm scale	μm to mm scale

[a] Step size is defined as one rotation of the 16HB body forward which matches the width of the square prism (10 nm)

[b] Processivity is defined as the number of steps taken before detachment from the track or starvation off the track. In our case, the 16HB motor can travel processively for multiple microns which matches hundreds of body lengths. Polyvalent DNA walkers gain processivity by having multiple footholds over unipedal DNA walkers. However, lack of coordination between DNA legs often results in track starvation and stalling of the DNA motor.

[c] Directionality is defined as having a preferred direction over multiple steps. Most DNA walkers be it unipedal, bipedal or polyvalent achieve minimal directionality through the burnt bridge mechanism by which they avoid the previous steps and move toward unconsumed substrate. This type of motion is called *self-avoiding*. However, the direction of the walking device can change due to random Brownian noise and will not be unidirectional. In many examples unidirectionality has been achieved through guidance of a track ^[9d, 12].

[d] The spherical nanoparticle motors display higher speeds but are not included in this comparison as they require further investigation.

16. Oligonucleotides used in this study

Supplementary Table 2. Oligonucleotide Sequences used in this study

ID	Sequence (5'-3')
DNA anchor	5AmMC6/GA GAG AGA TGG GTG CTT TTT TTT TTT TTT T/35OctdU/ [a]
RNA/DNA chimera substrate (fuel)	GCACCCATCTCTCTC <u>CrCrCrCrCrCrCrUrGrUrGrArUrUrGrArUrUrArCrU</u> /3Cy3Sp/ [b]
DNA legs	Origami Staple – TTTAGTAATCAATCACAG
Cargo binding strands	ATACATCTACTGTCGTGCCTC – Origami Staple
AF647 strand	GAGGCACGACAGTAGATGTAT /3AlexF647N/[c]
Thiolated DNA leg	/5ThioMC6-D/TTTTAGTAATCAATCACAG

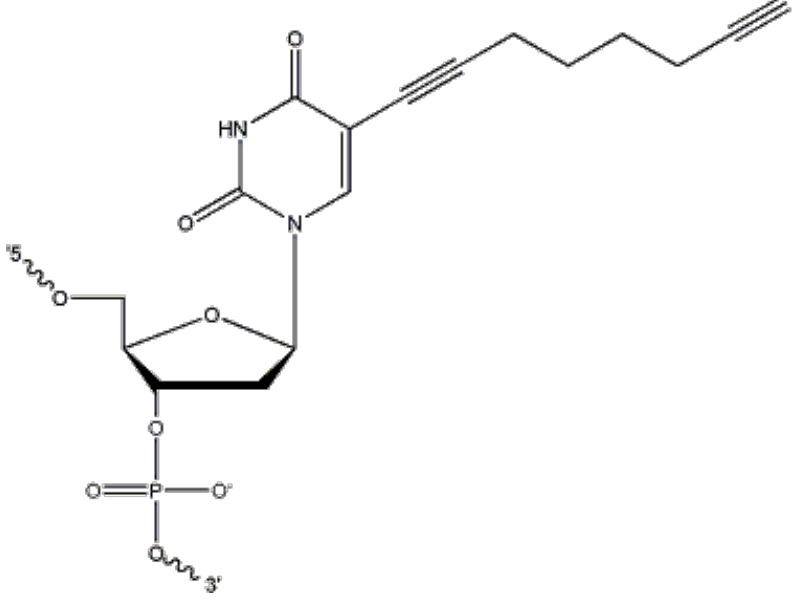
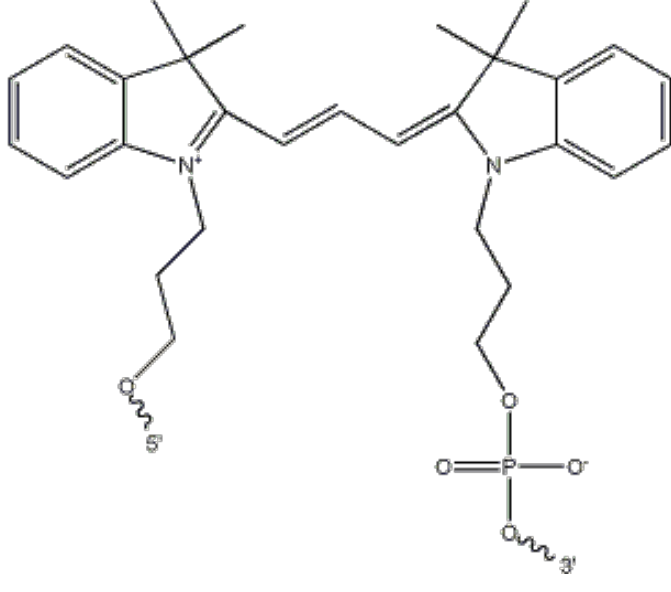
[a] The sequences are displayed in a 5' to 3' orientation. The anchor without amine lacks this 5AmMC6 modification.

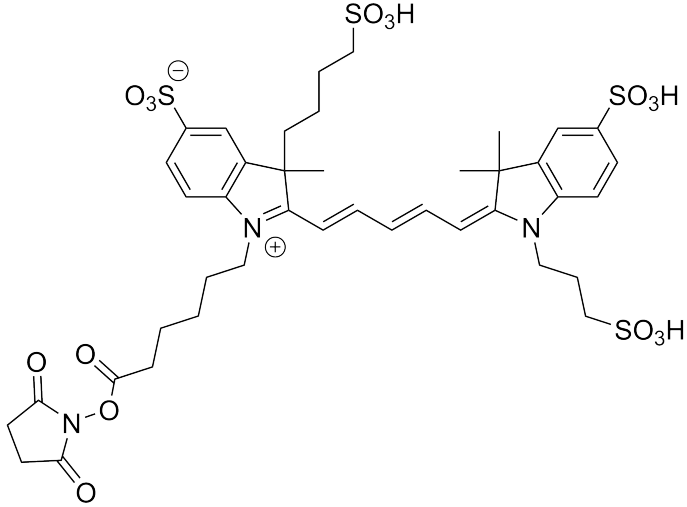
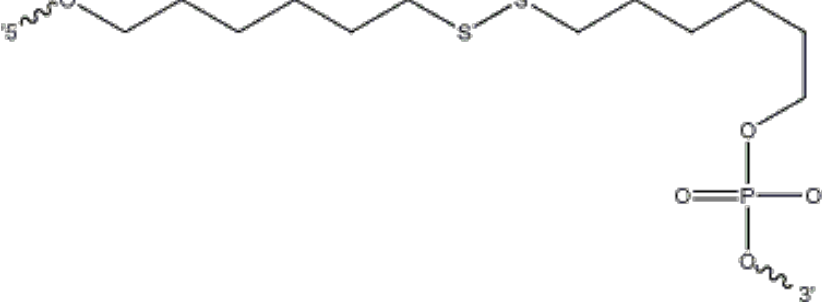
[b] The red text indicates RNA bases, and the underlined bases represent the RNase H recognition sequence.

[c] The 3' and 5' DNA and RNA modifications indicated in the table are illustrated in table S3.

Supplementary Table 3. Chemical structure of DNA and RNA modifications used in this study.

Modification ID	Modification name	Chemical Structure
5AmMC6	5' Amino modifier C6	

<p>35OctdU</p>	<p>3' 5- Octadiynyl dU</p>	
<p>3Cy3Sp</p>	<p>3'Cy3TM fluorescent dye</p>	

3AlexF647N	Alexa Fluor® 647(NHS Ester)	
5ThioMC6-D	5' Thiol Modifier C6 S-S	

Supplementary Table 4. Legend for notes on sequences used in 16HB design

16HB Design Legend

4-36	A
1-36	B
2c-36	C
2t-36	D
3-36	E
4-12	F
4-24	G
4-9	H
4-9+9	I
4-18	J

Supplementary Table 5. Sequences used in design of different 16HB motors

<i>Start</i>	<i>End</i>	<i>Sequence</i>	<i>Length</i>	<i>Notes</i>
0[71]	5[71]	AATAGTGACAAGACAAAATTCTGTTCGAGCCA	32	Blank
0[103]	5[103]	CGATAGCTATCGTCGCACAAAATCGAATTATT	32	Blank
0[135]	5[135]	TTTGATTACACTTGCCGAATGGCTTGCCAAC	32	Blank
0[167]	5[167]	ATCACGCAGCCTTGCTGGTTAAGAAAGCGTTG	32	Blank
0[199]	5[199]	AACCGTCTAGAGTCCAATTAATGATCTTTTCA	32	Blank
0[231]	5[231]	ATATGATACTAGCTGAGAGTAACAGCATTAAA	32	Blank
0[263]	5[263]	GAGAAAGGTATTTTTGGTAGCCAGTAACCAAT	32	Blank
0[295]	5[295]	TGAGTAATTCGGTTGTATTGCTGAGTAGCTCA	32	Blank
0[327]	5[327]	TTAGAACCTACTTTTGAGAGGTCAGTACGGTG	32	Blank
0[359]	5[359]	CCGATAGTATGACAACCTCATCTTAAATACGT	32	Blank
0[391]	5[391]	CTTTCGAGATATTCGGAGGCGAAATAAAAGTT	32	Blank
0[423]	5[423]	GGAGCCTTAGCGGAGTTGCTCAGTTGTATCAC	32	Blank
3[48]	5[63]	CCGGAATCATAATTACTTAATTCAGGCATTT	32	Blank
3[80]	5[95]	TAATTACATTTAACAAGTGAATAAAAGGAGGC	32	Blank
3[112]	5[127]	TTTTTAAATGGCATGGACGCTAAAGGACATTC	32	Blank
3[144]	5[159]	ACGCTCAATCGTCTGACAATATTATGACCTGA	32	Blank
3[176]	5[191]	TTGCCCCAGCAGGCGAAATAGCCCGTGGTTTT	32	Blank
3[208]	5[223]	TGGTTCCGAAACGTAAGTAATTCGTAAAATTC	32	Blank
3[240]	5[255]	ATATGTACCCCGTTGGAGTCTGGTCATTTTT	32	Blank
3[272]	5[287]	TCAATAACCTGTTTAGAGCCTCAGATAATGCT	32	Blank
3[304]	5[319]	GGCGGAGCTGAAAAGCAAGGCAACAATAAAA	32	Blank
3[336]	5[351]	TAATAGTAGTACAGCAACCTGCAAACGGGTA	32	Blank
3[368]	5[383]	GAACGAGGGTAGCAACAGGGAGTTCACCAACC	32	Blank
3[400]	5[415]	ACTGAGTTTCGTCACCATTTTCTGGGAATAGG	32	Blank
12[55]	9[55]	GAGCGTCTTGTTTAACTAAGAACTCATCGTA	32	Blank
12[87]	9[87]	TTCTGATTTACAGAGCAAAATCAAAGCAAAT	32	Blank
12[119]	9[119]	TAACCACCAGAAATAGCTGAATAAAGAAATTG	32	Blank
12[151]	9[151]	TTATCTAAATTTGAGGCTTGCTGAGTGCCACG	32	Blank
12[183]	9[183]	ATTTCTCCGTAAGCAACGTAATCATGTTTCCT	32	Blank
12[215]	9[215]	GACTGAATGGCCTGGCGACGGAGATTCCACA	32	Blank
12[247]	9[247]	CCAGGGTTGCCAGGGTGCTGCGCACTCCAGCC	32	Blank
12[279]	9[279]	GTAAGAGCATTTCATGCGAAAACCCGGATCC	32	Blank
12[311]	9[311]	ATACATAACAACATTACCAATACTGAAAACGA	32	Blank
12[343]	9[343]	CAGTTTAGTGAGATGAGGTAATAGGTCTTTAC	32	Blank
12[375]	9[375]	TTACCCAAACCAGAACACAGATGAAGACGGTC	32	Blank
12[407]	9[407]	CCGGAACCTAGCGACACTTGATATATAAAATCC	32	Blank
15[64]	9[79]	GAAACAATGAAATAGCACAGGGAACCAATAGC	32	Blank
15[96]	9[111]	AAGCCCTTTTTAAGAATAATTTTAAGAAATAA	32	Blank
15[128]	9[143]	GAACAAAGTTACCAGAAACTCGTACTGCAACA	32	Blank
15[160]	9[175]	GCAATAATAACGGAATCGACAGTGAATATAGC	32	Blank
15[192]	9[207]	ATGATTAAGACTCCTTTTTACGCTCGCTCACA	32	Blank
15[224]	9[239]	GCAAACGTAGAAAATATGTCGCGCAGATCGCA	32	Blank
15[256]	9[271]	AACATATAAAAGAAACTCCTTAGTTTCTGGTG	32	Blank
15[288]	9[303]	ATAAGTTATTTTGTGCTTGGGAAACAGTTCA	32	Blank
15[320]	9[335]	TCATATGGTTTACCAGTTTAAAGAAAAATCAG	32	Blank
15[352]	9[367]	GCGACATTCAACCGATAACTTTAACGAGGCGC	32	Blank
15[384]	9[399]	AATATTGACGAAATTTTCGATAGCAACAACAA	32	Blank
15[416]	9[439]	TTATCACCGTCACCGATAGCAAGGGGAAAGCGCAGTCTCT	32	Blank
6[87]	0[72]	CGACAAAACATCGGGAGACGCTGAGAAGAGTC	32	A,B,C,D,E,G,I
6[119]	0[104]	TTATGAATTGCTTATGATCTTTGAAAACATAG	32	A,B,C,D,E,F,G,I
6[151]	0[136]	CACAGACACGCCATTAGTTGTAGCAATACTTC	32	A,B,C,D,E,G,I
6[183]	0[168]	ACGCGCGGGTTGCGCTGTAAAAGAGTCTGTCC	32	A,B,C,D,E,F,G,I
6[215]	0[200]	GATTCGTGACCTGTCTACGTCAAAGGGCGAAA	32	A,B,C,D,E,G,J
6[247]	0[232]	AACATTAACCGTAATGAGTCAAATCACCATCA	32	A,B,C,D,E,F,G,J
6[279]	0[264]	CGCGTCTGTTCGAGCTAAAGATTCAAAGGGT	32	A,B,C,D,E,G,H,J
6[311]	0[296]	GATGGCTTAACTCCAATTTTAAATGCAATGCC	32	A,B,C,D,E,F,G,H,J
6[343]	0[328]	AGCGCTCCTAATTGATGCAAGGATAAAAAATTT	32	A,B,C,D,E,G,H,J
6[375]	0[360]	AGAATACAAACGGAGACTTAAACAGCTTGATA	32	A,B,C,D,E,F,G,I

6[407]	0[392]	GATAAGTGTGCCCCCTTCGGTATTATCAGCTTG	32	A,B,C,D,E,G,I
6[439]	0[424]	AGGATTAGGAAACATGAAAAAGGCTCCAAAA	32	A,B,C,D,E,F,G,I
11[80]	1[87]	ATGATGGCCAAGAAAAAGAATACCTACTTTAGAAATGC	40	A,B,C,D,E,I
11[112]	1[119]	TTTGGATTAATGAGCTTACCAAGCAGTACATAATTTTCC	40	A,B,C,D,E,I
11[144]	1[151]	AAATCAACATTGGCAGAACCTTCCCAGCAGAACTCA	40	A,B,C,D,E,I
11[176]	1[183]	TGAGTAAACCTGAGAGGCCAGGAGATAGGGTTCCAGT	40	A,B,C,D,E,J
11[208]	1[215]	GTTACCTCTTTCAACAACGGGTGTGCAAAATCGAACGTGG	40	A,B,C,D,E,J
11[240]	1[247]	GCCAGCTGATAAGCAAAAATCAGCAGCAAACATGCCGGAG	40	A,B,C,D,E,J
11[272]	1[279]	ATCATAACCATTCGCCATCAAAAAGCGGCTAACAAAATA	40	A,B,C,D,E,H,I
11[304]	1[311]	AACCAAAACGAACGAGTAAATATGAGAATTAGCATTATGA	40	A,B,C,D,E,H,I
11[336]	1[343]	GTTTTGCCCCATTCCATTTCAATTATAACATCGCCTTTAT	40	A,B,C,D,E,H,I
11[368]	1[375]	AGAGTAATTGAGGACTTACGAAGGAAAGGCCGCCACGCA	40	A,B,C,D,E,I
11[400]	1[407]	CAGAGCCGATAGCAAGTATAGCCCTATGGGATAACTTTCA	40	A,B,C,D,E,I
11[432]	1[439]	GAGCCACCCACCCTCAGGAGGTTTGTCTTTCCAAAGGAAC	40	A,B,C,D,E,I
8[79]	2[72]	CTTCAATCGAAACTTAGGTAAGTAGAACGCGTTCAAATA	40	A,B,C,D,E,F,G,I
8[111]	2[104]	TTTAACGTGCCTGATACCAAGTTTATTAATTAATCAAT	40	A,B,C,D,E,G,I
8[143]	2[136]	AAAACAGATAAAAACATATATTTTTTGGAGTAGACATTGCAA	40	A,B,C,D,E,F,G,I
8[175]	2[168]	TGAGTGAGTTAATTGCGGAGAGGCGGTGTGTTGTTGAAAT	40	A,B,C,D,E,G,J
8[207]	2[200]	GAAGCATAGTCGGGAACGAGCTGCCTATTAACCTTATAA	40	A,B,C,D,E,F,G,J
8[239]	2[232]	GTTGAGGCGGATTGAATGTGAGCTAAATTAAGAGAATC	40	A,B,C,D,E,G,J
8[271]	2[264]	TTTATGGGTGTAGTAAGCCTTCTAGAGATCTTCAGGTCA	40	A,B,C,D,E,F,G,H,J
8[303]	2[296]	AAGAGGAACGGAAGCAAGAGCTTAACCAAAAAACAAAATTA	40	A,B,C,D,E,G,H,J
8[335]	2[328]	TCAGAAGCAGTACCTTTTTTGATACGGGAGAACAATAAAT	40	A,B,C,D,E,F,G,H,J
8[367]	2[360]	AATCCGCGAAAGTACCTAAAACAAACCATCGCTTTTGCG	40	A,B,C,D,E,G,I
8[399]	2[392]	GTAACAGTACAGTTAACCGTCGAGTCGTAACCTTTGCCTG	40	A,B,C,D,E,F,G,I
8[431]	2[424]	GGTAATAAATTATCTCGGGGTTTGAATAGAGACGTTA	40	A,B,C,D,E,G,I
10[79]	3[79]	GATATAGAGTAATAAGCAATTTAGGCCCTGAAT	32	A,C,E,G,I
10[111]	3[111]	TGGAAGGGCATTTCAAAAAAGAGGAATTACC	32	A,C,E,F,G,I
10[143]	3[143]	ACCTCAAAGAGATAGATTACCAACATTTTG	32	A,C,E,G,I
10[175]	3[175]	TGGTCGAACGTATTGGAGTTGCAGACGCTGGT	32	A,C,E,F,G,I
10[207]	3[207]	ATCCCGGCCAGTGAGGCTGATTGTTTGATGG	32	A,C,E,G,J
10[239]	3[239]	ACTGTTGGTTTTTGTATATTTAATGTCAATC	32	A,C,E,F,G,J
10[271]	3[271]	GGCAAAGCAGGAACGCAAACCCCAAAAAGTGG	32	A,C,E,G,H,J
10[303]	3[303]	CGGAATCACATGTTTTAGATTTATCATTGG	32	A,C,E,F,G,H,J
10[335]	3[335]	TAAAATGTTCTGGAAGTATAACAGAAATTCTAC	32	A,C,E,G,H,J
10[367]	3[367]	ACGGTGTAAATGCCACAAAGACTTCAGCATCG	32	A,C,E,F,G,I
10[399]	3[399]	TCACATGAGATATAAGCCCAATAGACCGTAAC	32	A,C,E,G,I
10[431]	3[431]	GTTGAGGCCGTAAGTACAGAGCCACCCTACAACG	32	A,C,E,F,G,I
2[71]	4[64]	TATTTTAGTAGAAAAATATCATAT	24	A,C,E,I
2[103]	4[96]	ATATGTGATTTTCAATTTATGATGAA	24	A,C,E,I
2[135]	4[128]	CAGGAAAAAATACCTGTACACG	24	A,C,E,I
2[167]	4[160]	ATCCAGAAAATGGTCCCAACGCGGA	24	A,C,E,J
2[199]	4[192]	ATCAAAGAAATCCTGCCCTTAC	24	A,C,E,J
2[231]	4[224]	GATGAACGAACTAGCAATTGTA	24	A,C,E,J
2[263]	4[256]	TTGCTGAATAATCAGAAAACAGG	24	A,C,E,H,J
2[295]	4[288]	AGCAATAACTATATTTGTTGACC	24	A,C,E,H,J
2[327]	4[320]	CATACAGGGTGGCATCTTGATTCC	24	A,C,E,H,J
2[359]	4[352]	GGATCGTCGCGAAAGATTTACATGA	24	A,C,E,I
2[391]	4[384]	AGGCTTGCGGCCATGTGAACCTAC	24	A,C,E,I
2[423]	4[416]	GTAATGAAGTACAAAACCTCAT	24	A,C,E,I
13[72]	11[79]	AGCAGCCTTATCTGAATTATCCAG	24	A,C,E,F,G,I
13[104]	11[111]	CGGAACAAAGAAGGAGCCTGATTG	24	A,C,E,G,I
13[136]	11[143]	GATAATACAATATCTTCAGTTGGC	24	A,C,E,F,G,I
13[168]	11[175]	TGCCATCTGAACTCTGTGGTGTAA	24	A,C,E,G,J
13[200]	11[207]	AATATAGGCGGCTGACTGGTGCTT	24	A,C,E,F,G,J
13[232]	11[239]	CAGGAGAATTCCCAGTCTATTAC	24	A,C,E,G,J
13[264]	11[271]	GGTTGTGAAACAGGCGCTGCAACT	24	A,C,E,F,G,H,J
13[296]	11[303]	TAACGGAACGCCAAAAACGATAAA	24	A,C,E,G,H,J
13[328]	11[335]	TCATCAGTGAATACCACAAAAGAA	24	A,C,E,F,G,H,J
13[360]	11[367]	CGAGAAACATCAACGTCTTCATCA	24	A,C,E,G,I
13[392]	11[399]	GTAATCAGAGAGCCACGCCTCCCT	24	A,C,E,F,G,I
13[424]	11[431]	TAGCGTCAGCCATCTTCACCCTCA	24	A,C,E,G,I

10[71]	12[56]	AGGCTTATCTACAATTTCTTACCAACGCTAAC	32	A,D,E,G,I
10[103]	12[88]	TTAGAACCAATATAATCGGAATTATCATCATA	32	A,D,E,F,G,I
10[135]	12[120]	TATCAAACCTATCTGGTTAGGAGCACTAACAAAC	32	A,D,E,G,I
10[167]	12[152]	AAATCTAAGGACTGGTACCTCATTGAGGAAGG	32	A,D,E,F,G,I
10[199]	12[184]	GTACCGAGAAGCTACGGCATTTTCACATAAATCA	32	A,D,E,G,J
10[231]	12[216]	GAAGGGCGCCTCTTCCACGACGTTGTAAAAC	32	A,D,E,F,G,J
10[263]	12[248]	GCCATTTCGGGGATGTGATTAAGTTGGGTAACG	32	A,D,E,G,H,J
10[295]	12[280]	GTCATAAAACCAGACGGGAATTACGAGGCATA	32	A,D,E,F,G,H,J
10[327]	12[312]	TTAGACTGGGCTTTTGCATTCAACTAATGCAG	32	A,D,E,G,H,J
10[359]	12[344]	CAGACCAGTGGCTGACAACAAAGCTGCTCATT	32	A,D,E,F,G,I
10[391]	12[376]	CCAACTTTGAAGAACCCACCGCCGGATATTCA	32	A,D,E,G,I
10[423]	12[408]	AGGTCAGAAGAACCCTTCATAAATCAAAATCA	32	A,D,E,F,G,I
7[64]	13[71]	AGCATGTAATAATCGTACCCTGCGCATTAATGAAAAT	40	A,D,E,I
7[96]	13[103]	AACGGATTTCAGATGAACGTAAAACAAAGTTTGTGCTTTTG	40	A,D,E,I
7[128]	13[135]	GATAGCCCCGTGAGGCAACACCGCTTAAATCCCGTCAATA	40	A,D,E,I
7[160]	13[167]	GAATCACACTAACCGACAGCAGCAGCGGAGACTGTATTCCC	40	A,D,E,J
7[192]	13[199]	GCTTTCCAAAGTGTAATTGTATCCGCCCTGGTGGGCACG	40	A,D,E,J
7[224]	13[231]	ACAAACGGGGACGACGCCTCAGGACAAAATAAAGCTTTCT	40	A,D,E,J
7[256]	13[263]	CACGTTGGCGCATCGTGGCACCCGCTGAATTTTCTAAGT	40	A,D,E,H,J
7[288]	13[295]	AACCAGACGCCCCGAAATGCTTTAAGAAAAATCAAACGAAC	40	A,D,E,H,J
7[320]	13[327]	GATTAGAGAAAGCGGAATAAATCACTGGCTCAAGAAAGAT	40	A,D,E,H,J
7[352]	13[359]	GCGCGAAAACCTGCTCAGCCGGAATCATTGTGTGCCCTGA	40	A,D,E,I
7[384]	13[391]	ATCTATAAGCCCAGCCGGGAACCGAGCGGCTTAATTGACC	40	A,D,E,I
7[416]	13[423]	CGGAACCTGTTTTAACGCCAGAATCCGGAACCTTTGCCCTT	40	A,D,E,I
4[63]	14[56]	GCGTTATAGCACCCAGCCGGTATTCGTCAAAAGACGGGGAG	40	A,D,E,F,G,I
4[95]	14[88]	ACAAACATAAATTCATCTACCATAATAGACATTAAGTAAATA	40	A,D,E,G,I
4[127]	14[120]	ACCAGTAAATAATCAACCTCACTATTAGAGCTTTGCCCCG	40	A,D,E,F,G,I
4[159]	14[152]	TTATTTACAGTTGAAAAGCATCACATTTAGAAATTACAAAC	40	A,D,E,G,J
4[191]	14[184]	CGCCTGGCCAGGGCTTCTCGAATTCTCGTCGGAGTGACTC	40	A,D,E,F,G,J
4[223]	14[216]	CGTTAATAGATTGCGGATCGGAAACAGTGCCACCCCGCTT	40	A,D,E,G,J
4[255]	14[248]	AAGATTGTGCGAAAGGCCATTACAGGGATGTTTCGTCAACCT	40	A,D,E,F,G,H,J
4[287]	14[280]	ATTAGATACCTCGTTTTATTTCATTGCATAATATACGTCGA	40	A,D,E,G,H,J
4[319]	14[312]	CAATTCTGTAGCGAGAGATAGCGTTTACAGGTTTATACCA	40	A,D,E,F,G,H,J
4[351]	14[344]	GGAAGTTTAGATAGGCGCGCAGGGATAAAGGCTAATTACCT	40	A,D,E,G,I
4[383]	14[376]	AGAGGCTTCTTGACAAGAAAGAGGGAGTAGTAGAGATGGT	40	A,D,E,F,G,I
4[415]	14[408]	TTTCAGGGCCACCCTCCGATTGGCGAATCAAGGTCACCAA	40	A,D,E,G,I
6[63]	15[63]	CCAGACGAGGAATCATGCTGTCTTAAGAGCAA	32	A,G,I
6[95]	15[95]	GCGCATACTATTTGCATATACAGTTCTTACCG	32	A,F,G,I
6[127]	15[127]	ATTAGTCTCGTGTATTGGTCAAGAAGATAGCC	32	A,G,I
6[159]	15[159]	ATACGTGGCTGAGAGCACCACCGAGGAGGAAAC	32	A,F,G,I
6[191]	15[191]	ATCGGCCAGTGTGAAAAGCCTGGGGAACCTGGC	32	A,G,J
6[223]	15[223]	ACCCGTCGCAAATCGGACAGTCATGTATGTTA	32	A,F,G,J
6[255]	15[255]	CTTTCATCAGCTTTCCAACCGTGCAAGGTGGC	32	A,G,H,J
6[287]	15[287]	ATATAATTCCTCAAAGACTTCAAACCACGGA	32	A,F,G,H,J
6[319]	15[319]	TTTTTGCGGAATGACCTTGCATCATAGAAAAT	32	A,G,H,J
6[351]	15[351]	TGACCCCCCTTACTTCATGTGACACAAAAGG	32	A,F,G,I
6[383]	15[383]	GAGGCAAAAATCATAATGATAAATGGAAGGTA	32	A,G,I
6[415]	15[415]	ACCAGGCGTCATTAAGGGGTCAGAAGGTGAA	32	A,F,G,I
14[55]	8[47]	AATTAACCTCCAATAATTCCTTATCA	25	A,I
14[87]	8[80]	ACATAAAAAATAGCTAAACAGTAC	24	A,I
14[119]	8[112]	AACGTTATAAGTAAGCTTTTCAGG	24	A,I
14[151]	8[144]	AATTCGACAGGAAACCCAGAAGAT	24	A,J
14[183]	8[176]	TATGATACACCCAAAAGTGCCTAA	24	A,J
14[215]	8[208]	CTAATCTAATTACGCAACGAGCCG	24	A,J
14[247]	8[240]	TATGACAACATACATAATCTGCCA	24	A,H,J
14[279]	8[272]	CTTAAGTGGCAAAGACATAATCGCG	24	A,H,J
14[311]	8[304]	GTCAGGACACAATCAAAAAGATT	24	A,H,J
14[343]	8[336]	TATGCGATCGCCAAAGTATTATAG	24	A,I
14[375]	8[368]	TTAATTTCTGAGGGAGTGTGTCGA	24	A,I
14[407]	8[400]	TGAAACCAATTCATTATGCCTTGA	24	A,I
1[56]	7[63]	TCCAATCGATTATCAAATTTACG	24	A,F,G,I
1[88]	7[95]	TTCTGTAATAGATTAAGAAACAAT	24	A,G,I

1[120]	7[127]	CTTAACATGTAATAGACGCGAACT	24	A,F,G,I
1[152]	7[159]	AACTATCGAATTAACCAAAATACC	24	A,G,J
1[184]	7[191]	TTGGAACAATCACCGACACTGCC	24	A,F,G,J
1[216]	7[223]	ACTCCGTTTTCAACCACCGTGGGA	24	A,G,J
1[248]	7[255]	AGGGTAGCCCGGAGACGGATAGGT	24	A,F,G,H,J
1[280]	7[287]	AAGCTAAAGTGTAGTTCAAAGCG	24	A,G,H,J
1[312]	7[319]	CCCTGTAACTCATATACAGGTCAG	24	A,F,G,H,J
1[344]	7[351]	TTCCGACATGCGCAACTATACCAA	24	A,G,I
1[376]	7[383]	TAACCGATGTGAATTTTTGTATC	24	A,F,G,I
1[408]	7[415]	ACAGTTTCTAATTGTAGCCTATTT	24	A,G,I
0[463]	0[440]	TTTTTTCACGTTGAAAATCTCAA	24	Cargo-Binding Strand
2[463]	2[440]	AGCGTAACGATCTAAAGTTTTGTC	24	Cargo-Binding Strand
4[458]	4[440]	CCGCCACCCTCAGAACCGC	19	Cargo-Binding Strand
6[458]	6[440]	ACTCCTCAAGAGAAGGATT	19	Cargo-Binding Strand
8[463]	8[440]	ATACATGGCTTTTGATGATACAGG	24	Cargo-Binding Strand
10[463]	10[440]	ACCACCAGAGCCGCCGCGCAGCATT	24	Cargo-Binding Strand
12[458]	12[435]	TCGGTCATAGCCCCCTATTAGCG	24	Cargo-Binding Strand
14[458]	14[435]	CAAAATCACCAGTAGCACCATTAC	24	Cargo-Binding Strand
1[16]	1[47]	TAGGTTGGGTTATATAACTATATGTAATGCT	32	Cargo-Binding Strand
3[16]	3[47]	GTGATAAATAAGGCGTTAAATAAGAATAAACA	32	Cargo-Binding Strand
5[11]	5[43]	TTGAGAATCGCCATATTTAACAACGCCAACATG	33	Cargo-Binding Strand
7[11]	7[43]	TCAACAATAGATAAGTCCTGAACAAGAAAAATA	33	Cargo-Binding Strand
9[16]	9[47]	ACTCATCGAGAACAAGCAAGCCGTTTTTATTT	32	Cargo-Binding Strand
11[16]	11[47]	GGAGGTTTTGAAGCCTTAAATCAAGATTAGTT	32	Cargo-Binding Strand
13[11]	13[43]	CATATTATTTATCCCAATCCAAATAAGAAACGA	33	Cargo-Binding Strand
15[11]	15[43]	AATATCAGAGAGATAAACCACAAGAATTGAGTT	33	Cargo-Binding Strand

17. Captions for supplementary movies

Supplementary Movie 1: A representative time lapse video in the TIRF647 channel showing 16HB origami motors binding to an RNA surface. Imaging was initiated after adding a 10 pM solution of AF647-16HB in 1X RNase H buffer to the RNA surface. The images were acquired using a 100x 1.49 NA objective at a frequency of two per min for a duration of 5 minutes. Scale bar is 10 μm . Note that these are individual origami structures that are binding to the surface and hence becoming visible via 647 TIRF imaging. These are not fluorescence blinking events.

Supplementary Movie 2: A representative time lapse video of the TIRF647 and Cy3 channels overlaid showing AF647-16HB motor motion on Cy3-RNA surface. TIRF647 channel is shown in gray while the cy3 channel is shown in red. Images were acquired using a 100x 1.49 NA objective at 30 s intervals for a duration of 63 min. 16HB structures were hybridized to the RNA surface and treated with a solution of 1X RNase H buffer (3 mM Mg^{2+} , 1 mM DTT, 5% v/v formamide and 43.2 nM RNase H). Scale bar is 10 μm .

Supplementary Movie 3: A representative time lapse video of the TIRF647 and Cy3 channels overlaid showing a single AF647-16HB motor on the Cy3-RNA surface. TIRF647 channel is shown in gray while the cy3 channel is shown in red. Images were acquired using a 100x 1.49 NA objective at 30 s intervals for a duration of 60 min. 16HB structures were hybridized to the RNA surface and treated with a solution of 1X RNase H buffer (3 mM Mg^{2+} , 1 mM DTT, 5% v/v formamide and 43.2 nM RNase H). Scale bar is 10 μm .

Supplementary Movie 4: A representative time lapse video of spherical nanomotors moving on an RNA surface. Images were acquired in the RICM channel using a 100x 1.49 NA (with 1.5X zoom) objective at 5 second intervals for 15 minutes. Spherical nanomotors were hybridized to the RNA surface and treated with 0.5X RNase H buffer, 10 μM DTT, 10 % v/v formamide and 0.75% v/v triton X and 72 nM RNase H. Scale bar is 10 μm .

18. References

- [1] G. Bellot, M. A. McClintock, J. J. Chou, W. M. Shih, *Nat Protoc* **2013**, *8*, 755-770.
- [2] S. M. Douglas, A. H. Marblestone, S. Teerapittayanon, A. Vazquez, G. M. Church, W. M. Shih, *Nucleic Acids Res* **2009**, *37*, 5001-5006.
- [3] B. Liu, J. Liu, *Journal of the American Chemical Society* **2017**, *139*, 9471-9474.
- [4] I. F. Sbalzarini, P. Koumoutsakos, *Journal of Structural Biology* **2005**, *151*, 182-195.
- [5] J. Schnitzbauer, M. T. Strauss, T. Schlichthaerle, F. Schueder, R. Jungmann, *Nature Protocols* **2017**, *12*, 1198.
- [6] A. Rizk, G. Paul, P. Incardona, M. Bugarski, M. Mansouri, A. Niemann, U. Ziegler, P. Berger, I. F. Sbalzarini, *Nature Protocols* **2014**, *9*, 586.
- [7] R. D. Blake, S. G. Delcourt, *Nucleic Acids Res.* **1996**, *24*, 2095-2103.
- [8] K. D. Whitley, M. J. Comstock, Y. R. Chemla, *Nucleic Acids Res.* **2017**, *45*, 547-555.
- [9] a) Y. He, D. R. Liu, *Nat Nanotechnol* **2010**, *5*, 778-782; b) J.-S. S. and, Niles A. Pierce*, ‡, **2004**; c) C. Jung, P. B. Allen, A. D. Ellington, *Nat Nano* **2016**, *11*, 157-163; d) P. Yin, H. Yan, X. G. Daniell, A. J. Turberfield, John H Reif, *Angewandte Chemie International Edition* **2004**, *43*, 4906-4911; e) T. Omabegho, R. Sha, N. C. Seeman, **2009**.
- [10] a) T.-G. Cha, J. Pan, H. Chen, J. Salgado, X. Li, C. Mao, J. H. Choi, *Nature Nanotechnology* **2013**, *9*, 39; b) H. Gu, J. Chao, S.-J. Xiao, N. C. Seeman, *Nature* **2010**, *465*, 202; c) K. Lund, A. J. Manzo, N. Dabby, N. Michelotti, A. Johnson-Buck, J. Nangreave, S. Taylor, R. Pei, M. N. Stojanovic, N. G. Walter, E. Winfree, H. Yan, *Nature* **2010**, *465*, 206; d) C. Zhou, X. Duan, N. Liu, *Nature Communications* **2015**, *6*, 8102; e) J. Pan, T. G. Cha, F. Li, H. Chen, N. A. Bragg, J. H. Choi, in *Sci Adv*, *Vol. 3*, **2017**.
- [11] a) R. D. Vale, T. Funatsu, D. W. Pierce, L. Romberg, Y. Harada, T. Yanagida, *Nature* **2019**, *380*, 451;
- [12] K. Lund, A. J. Manzo, N. Dabby, N. Michelotti, A. Johnson-Buck, J. Nangreave, S. Taylor, R. Pei, M. N. Stojanovic, N. G. Walter, E. Winfree, H. Yan, *Nature* **2010**, *465*, 206-210.